

THE SHUTTLE RADAR TOPOGRAPHY MISSION

Tom G. Farr,¹ Paul A. Rosen,¹ Edward Caro,¹ Robert Crippen,¹ Riley Duren,¹ Scott Hensley,¹ Michael Kobrick,¹ Mimi Paller,¹ Ernesto Rodriguez,¹ Ladislav Roth,¹ David Seal,¹ Scott Shaffer,¹ Joanne Shimada,¹ Jeffrey Umland,¹ Marian Werner,² Michael Oskin,³ Douglas Burbank,⁴ and Douglas Alsdorf⁵

Received 13 September 2005; revised 27 September 2006; accepted 14 November 2006; published 19 May 2007.

[1] The Shuttle Radar Topography Mission produced the most complete, highest-resolution digital elevation model of the Earth. The project was a joint endeavor of NASA, the National Geospatial-Intelligence Agency, and the German and Italian Space Agencies and flew in February 2000. It

used dual radar antennas to acquire interferometric radar data, processed to digital topographic data at 1 arc sec resolution. Details of the development, flight operations, data processing, and products are provided for users of this revolutionary data set.

Citation: Farr, T. G., et al. (2007), The Shuttle Radar Topography Mission, *Rev. Geophys.*, 45, RG2004, doi:10.1029/2005RG000183.

1. INTRODUCTION

1.1. Need for Global Topography

[2] At the foundation of modern geosciences, quite literally, is knowledge of the shape of the Earth's surface. From hydrologic models of flooding and runoff to atmospheric boundary layer friction theories the Earth's topography is an essential constraint and boundary condition. There is an obvious practical importance to a high-quality global digital elevation model (DEM) as well. Elevation models, in the form of topographic maps, provide a base and context for airborne navigation systems and for a range of field activities in the civilian and military sectors.

[3] Conventional topographic mapping technologies have produced maps of uneven quality: some with astounding accuracy, some far less adequate. Most industrial countries have created and maintain national cartographic databases. The map products derived from these databases have demonstrated the idiosyncrasies of these conventional topographic data: The maps are at a variety of scales and resolutions, often referenced to country-specific datums and thus are inconsistent across national boundaries. Furthermore, the global coverage has been uneven. In many parts

of the world, particularly cloudy parts of South America and Africa, very little high-quality topographic data exist.

[4] It has proven exceedingly difficult and expensive to produce a global map set or digital elevation model of consistent scale and resolution by conventional means. The cost of deploying aircraft globally is prohibitive, and many areas are inaccessible politically. Optical stereo mapping systems suffer from poor control and matching difficulties in areas of low contrast and from persistent cloud cover in many important areas of the world.

[5] The only practical way to produce a globally consistent topographic data set is by employing a globally consistent mapping technique. The emergence, in the 1990s, of synthetic aperture radar (SAR) interferometry [Zebker and Goldstein, 1986; Massonnet, 1997; Madsen and Zebker, 1998; Rosen et al., 2000] placed the possibility of efficiently and affordably creating a global digital elevation model within the grasp of spacefaring nations. The Shuttle Radar Topography Mission (SRTM) demonstrated the power of the new technique (Figure 1).

[6] Interferometric SAR, or InSAR, makes use of phase-difference measurements derived from two radar images acquired with a very small base to height ratio (typically 0.0002) to measure topography. Accuracy is obtained by careful measurement of the baseline length and orientation and the location of the platform relative to the reference coordinate system. As radar wavelengths in the centimeter to meter range furnish good signal returns from rough surfaces such as bare ground, rough water, and vegetation, these surfaces are what is represented by the DEM. In particular, heavy vegetation canopies may not be penetrated significantly, and the topographic map will not correspond

¹Jet Propulsion Laboratory, California Institute of Technology, Pasadena, California, USA.

²Deutsches Zentrum für Luft- und Raumfahrt, Wessling, Germany.

³Department of Geological Sciences, University of North Carolina, Chapel Hill, North Carolina, USA.

⁴Department of Earth Science, University of California, Santa Barbara, California, USA.

⁵School of Earth Sciences, Ohio State University, Columbus, Ohio, USA.

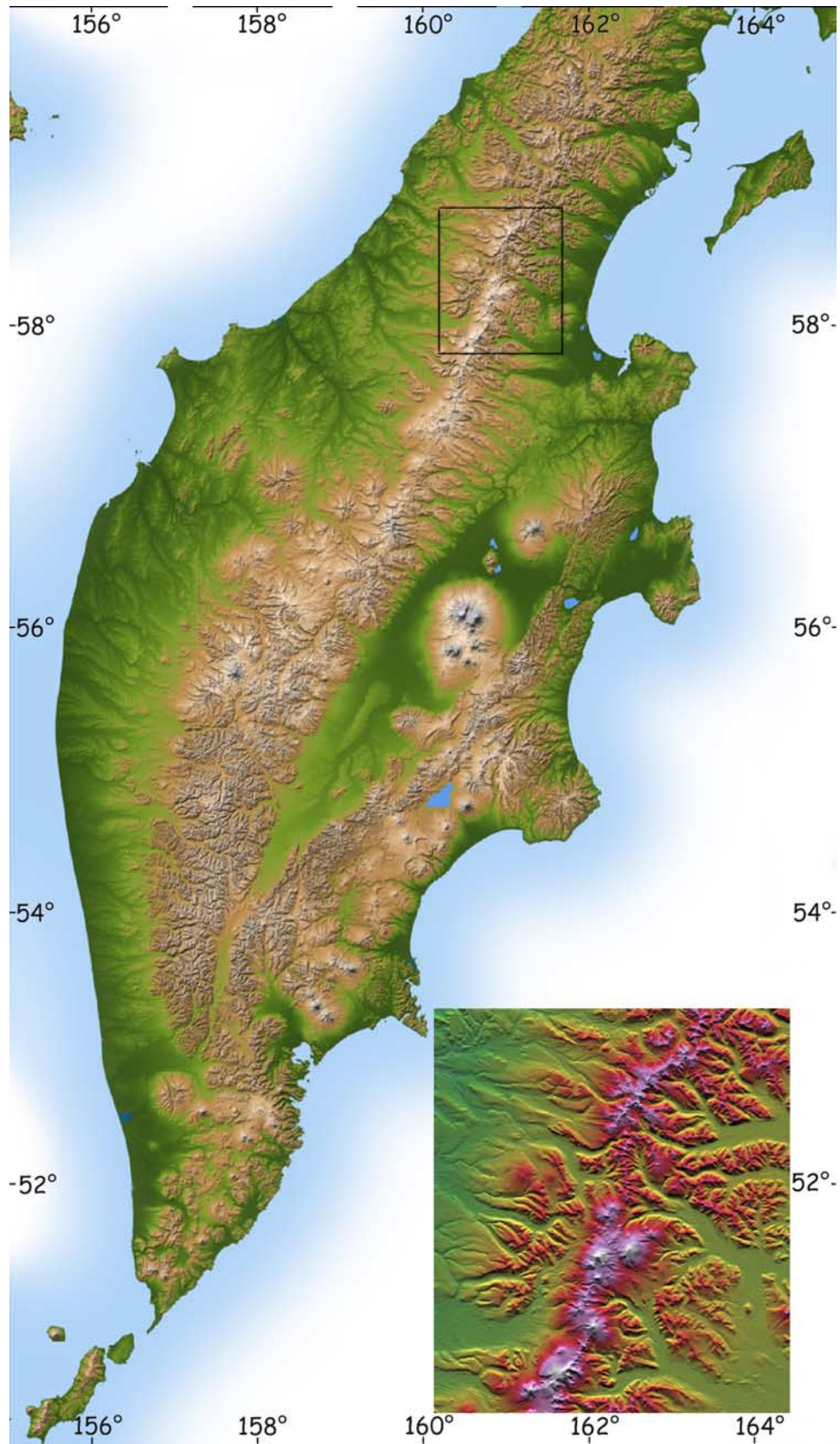


Figure 1. SRTM shaded-relief topographic rendering of the Kamchatka Peninsula. Inset shows a higher-resolution view of the boxed area, with a different color table to emphasize geomorphic features. Large image is 638 × 1113 km; inset is 93 × 106 km; north is up. Jet Propulsion Laboratory images PIA03314 and PIA03374. Courtesy NASA/JPL-Caltech.

to the ground surface in those areas. In addition, smooth surfaces such as calm water and smooth sand sheets may not scatter enough radar energy back to the sensor and thus may not yield a height measurement.

1.2. Genesis of SRTM: The Shuttle Imaging Radar Program

[7] When the space shuttle became operational, it ushered in a new era of conducting remote sensing missions from low Earth orbit aboard a reusable spacecraft that had onboard accommodations unlike any spacecraft that had flown before. On its flight in 1981 the shuttle carried the first science payload, OSTA-1 (Office of Space and Terrestrial Applications-1), including a synthetic aperture radar, designated Shuttle Imaging Radar-A (SIR-A). The SIR-A instrument was a singly polarized (horizontal send and receive (HH)) L band (23.5 cm wavelength) SAR with a fixed look angle of 45° off nadir [Elachi et al., 1982].

[8] SIR-B, which flew on Challenger mission 41-G (5–13 October 1984), was the next step in the evolution of shuttle-borne radars. System upgrades included a foldable antenna with the addition of a mechanical pointing system that allowed the beam to be steered over a look angle range of 15° to 60° . Like its predecessor, SIR-B operated at L band and was HH polarized [Elachi et al., 1986].

[9] SIR-C was proposed as a development tool to address the technical challenges posed by a multifrequency, multi-polarization SAR with wide-swath capability. After considerable study and development through much of the 1980s the SIR-C instrument evolved into SIR-C/X-SAR, an L band and C band (5.6 cm) fully polarimetric radar with electronic scanning capability, coupled with an X band (3.1 cm) single-polarization (vertical send and receive (VV)) mechanically steered radar supplied by the German Aerospace Center (Deutsches Zentrum für Luft- und Raumfahrt (DLR)) and the Italian Space Agency (Agenzia Spaziale Italiana (ASI)). SIR-C/X-SAR flew as the Space Radar Laboratory (SRL) in April and October 1994 [Evans et al., 1997; Jordan et al., 1995]. SRL-1 and SRL-2 gathered images over predesignated target sites and exercised several experimental SAR techniques. Among the SIR-C/X-SAR experiments were successful demonstrations of repeat-pass interferometry, where images of a target were obtained on repeat orbits (the difference in positions on each pass forming the interferometric baseline) [Fielding et al., 1995; Coltelli et al., 1996; Rosen et al., 2000], and ScanSAR, where radar beams were electronically steered in elevation to increase the swath width. ScanSAR interferometric operations were the basis of the SRTM topographic measurement scheme.

1.3. SRTM Objectives and Performance Requirements

[10] The Shuttle Radar Topography Mission, flown on Space Shuttle Endeavour in February 2000 (STS-99), was a joint project of the National Aeronautics and Space Administration, the National Geospatial-Intelligence Agency (NGA) (formerly National Imagery and Mapping Agency (NIMA)) of the U.S. Department of Defense (DOD), and

DLR [Farr and Kobrick, 2000; Werner, 2001]. DLR worked in partnership with ASI. The SRTM objective was to acquire a digital elevation model of all land between about 60° north latitude and 56° south latitude, about 80% of Earth's land surface. In quantitative terms the cartographic products derived from the SRTM data were to be sampled over a grid of 1 arc sec by 1 arc sec (approximately 30 m by 30 m), with linear vertical absolute height error of less than 16 m, linear vertical relative height error of less than 10 m, circular absolute geolocation error of less than 20 m, and circular relative geolocation error of less than 15 m. The relative height error of the X band SRTM data was to be less than 6 m. All quoted errors are at 90% confidence level, consistent with National Map Accuracy Standards (NMAS). These specifications are similar to those of the 30-m DEMs produced by the U.S. Geological Survey as part of the National Elevation Dataset (NED) [Gesch et al., 2002]. NED was produced by photogrammetric reduction of stereo air photographs yielding generally a representation of the elevations of the ground surface even beneath vegetation canopies. As discussed in section 5.1.7, the SRTM radars were unable to sense the surface beneath vegetation canopies and so produced elevation measurements from near the top of the canopies.

1.4. Mission Overview

[11] SRTM employed two synthetic aperture radars, a C band system (5.6 cm, C radar) and an X band system (3.1 cm, X radar). NASA's Jet Propulsion Laboratory (JPL) was responsible for C radar. The DLR with Astrium (formerly Dornier Satellitensysteme, GmbH), its contractor for the X band space segment, was responsible for X radar. The operational goal of C radar was to generate contiguous mapping coverage as called for by the mission objectives. X radar generated data along discrete swaths 50 km wide. These swaths offered nearly contiguous coverage at higher latitudes [Foni and Seal, 2004].

[12] X radar was included as an experimental demonstration. As it did not employ ScanSAR, the X band radar had a slightly higher resolution and better signal-to-noise ratio (SNR) than the C band system. Thus it could be used as an independent data set to help resolve problems in C radar processing and quality control [Hoffmann and Walter, 2006].

[13] The SIR-C/X-SAR interferometric experiments, along with numerous repeat-pass interferometry results from Seasat [Zebker and Goldstein, 1986] and the European Remote Sensing Satellite (ERS) missions [e.g., Attema, 1991; Zebker et al., 1994; Ruffino et al., 1998; Sansosti et al., 1999] showed that regional topographic mapping is possible using the repeat-pass technique but that inherent to repeat-pass radar interferometry are serious limits to the quality of the data, which then lead to difficulties in automating the production. Among these are temporal atmospheric changes from pass to pass, uncertainties in the orbit of the satellite, necessitating estimation of the interferometric geometry from the data themselves, and decorrelation of the radar echoes from pass to pass because of rearrangement of scatterers on the surface [Goldstein,

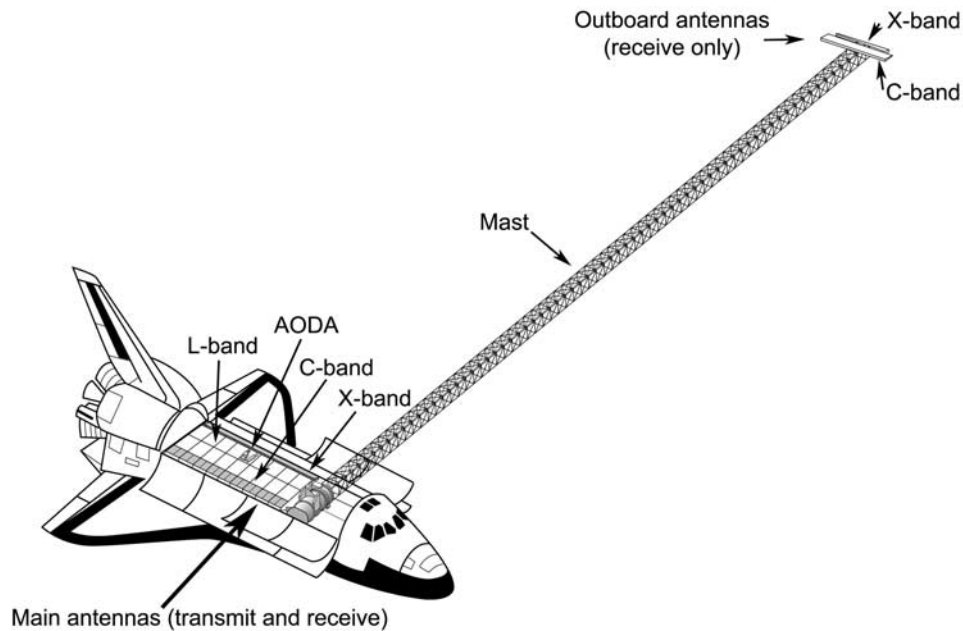


Figure 2. Major components of SRTM. In the shuttle payload bay are the main antennas (L band was not used) and the attitude and orbit determination avionics (AODA). At the end of the 60-m-long mast are the secondary antennas.

1995; Massonnet and Feigl, 1995; Zebker et al., 1997]. As evidence of these difficulties it should be noted that despite over 12 years of worldwide acquisition of satellite data suitable for repeat-pass interferometry, an acceptable global DEM has not been produced using repeat-pass InSAR.

[14] The key to successful acquisition of a data set suitable for automated production is to remove the variability and decorrelation due to pass-to-pass observations and to measure the interferometer baseline and other systematic effects accurately at all times during data acquisition. Therefore the SRTM radars were designed to operate as single-pass interferometers, utilizing the SRL C and X band capabilities. For single-pass interferometry operations each of the two SRTM radars was equipped with a supplementary receive-only antenna in addition to the main transmit/receive antennas situated in the shuttle's payload bay. The supplementary antennas were placed at the end of a retractable 60-m mast (Figure 2). During the shuttle launch and landing the mast was stowed in a canister attached to the forward edge of the main antenna assembly.

[15] Endeavour was launched with a six-person crew from the Kennedy Space Center (KSC) on 11 February 2000, 1744 Greenwich mean time (GMT). The nominal altitude was chosen to be 233 km; the orbital inclination was 57° . With this geometry the shuttle would begin repeating in 159 orbits in about 10 days. Since individual orbits were separated by 218 km at the equator and since, fortuitously, the width of the ScanSAR imaging swath was 225 km, Endeavour could map the target area, the strip between 60° north latitude (the southern tip of Greenland) and 56° south (Tierra del Fuego), in a single cycle of 159 orbits.

[16] Following the launch, the first 12 hours of flight were taken up by on-orbit checkout (OOCO), during which the payload bay doors were opened, the SRTM system was activated and checked, and the orbiter was maneuvered to the mapping attitude. With the successful acquisition and verification of test data, SRTM radar mapping began. Mapping continued for 149 orbits (222.4 hours). Data were acquired at the rate of 180 megabits per second (Mbps) (C radar) and at 90 Mbps (X radar). Both rates were higher than the shuttle's down link capacity (45 Mbps). This required the use of high-rate data tape recorders. Selected snapshots of data necessary for near-real-time performance assessment were down linked via the shuttle Ku band and NASA's tracking and data relay system (TDRS) link to JPL in Pasadena and to the Payload Operations Control Center (POCC) in Houston. The total SRTM raw data volume amounted to 12.3 Tb. About 99.96% of the targeted area was mapped by the C radar at least once (Figure 3a). Because of the loss of 10 orbits, a few patches of land in North America were missed. The X radar data cover about 40% of the target area (Figure 3b). Data gathering was concluded on flight day 10. Endeavour landed at KSC on 22 February 2000, 2322 GMT.

1.5. Techniques

[17] Radars at their most basic are instruments that measure only one dimension: the range from the radar to a target of interest. A radar instrument mounted on a moving platform can form two-dimensional measurements of a target location by exploiting the Doppler frequency shift of a given target as well as its range. This synthetic aperture radar technique yields two-dimensional images that are resolved in range proportional to the reciprocal of the

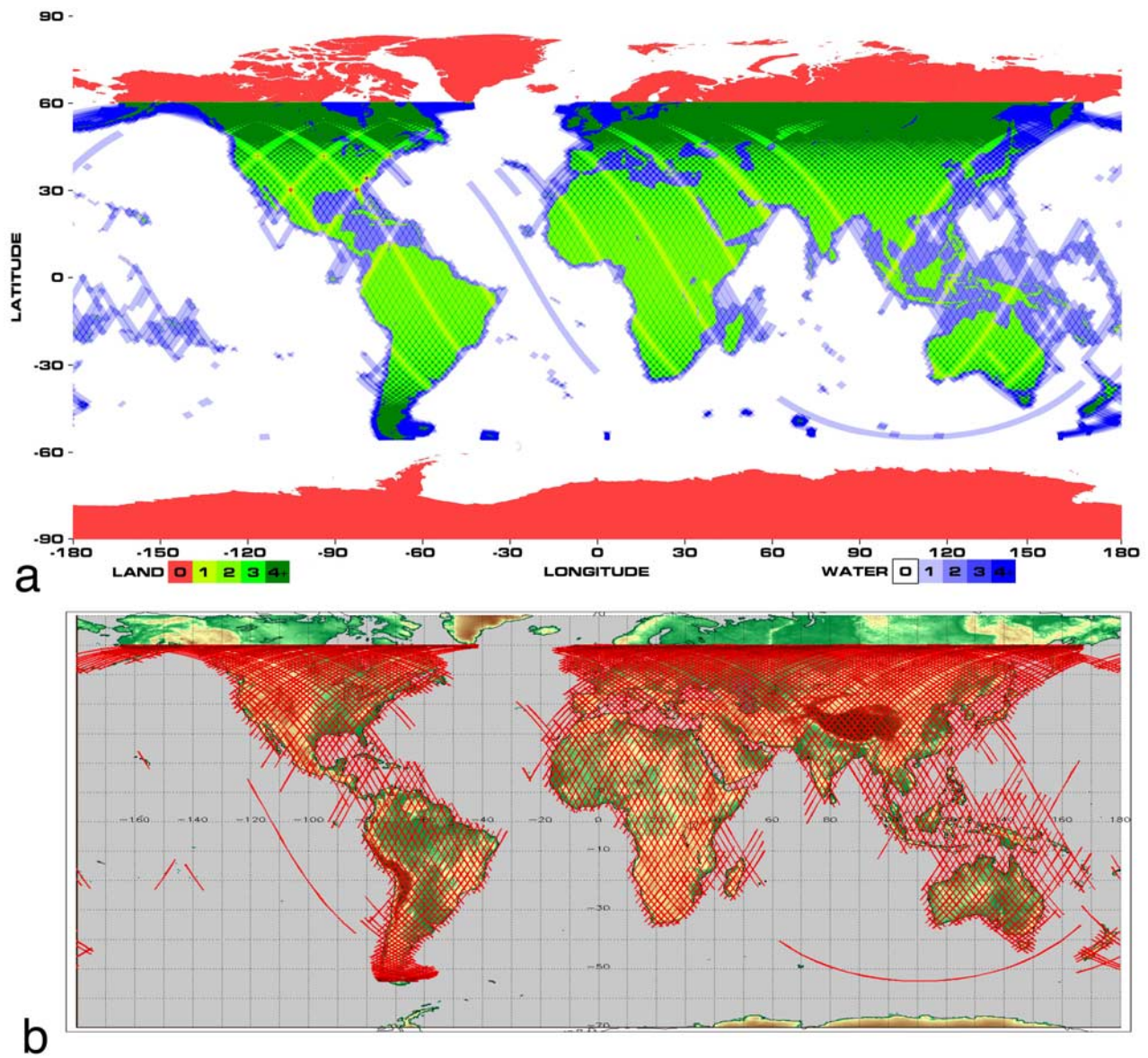


Figure 3. Final coverage maps for the (a) C band and (b) X band systems. The radars operated virtually flawlessly; C band imaged 99.96% of the targeted landmass at least one time, 94.59% at least twice, and about 50% at least three or more times. Note small red areas in the United States indicating missed areas, as well as the polar areas that could not be reached by the shuttle’s orbit. The X band system, because it did not operate in scanSAR mode, collected 50-km swaths with gaps between them. These gaps closed up at higher latitudes.

radar bandwidth and in azimuth equal to half the antenna length in the direction of motion. Typically, this leads to images from space with 5- to 10-m resolution when the radar is operated in this conventional strip-mapping mode [e.g., *Elachi*, 1988; *Raney*, 1998].

[18] To access the third dimension, a range difference between two radar images is required, and this is realized most accurately and efficiently using principles of interferometry, Figure 4 illustrates the concept of radar interferometry. Each radar antenna images the surface from a slightly different vantage point. The radar is a phase-coherent imaging system, and the phase of the radar signal encodes the path distance to the surface and back as well as any

phase imparted by backscatter from the surface. If the images from two antennas are acquired simultaneously and from close enough vantage points, the backscatter phase observed in both images from each point on the ground will be the same. The phase difference between each image point will then simply be the path difference between the two measurements of the point. Assuming the position of the two antennas (the “interferometric baseline”) is known, the dimensions of the interferometric triangle can be determined accurately and so also the height of a given point (Figure 4) [e.g., *Massonnet*, 1997; *Madsen and Zebker*, 1998; *Rosen et al.*, 2000].

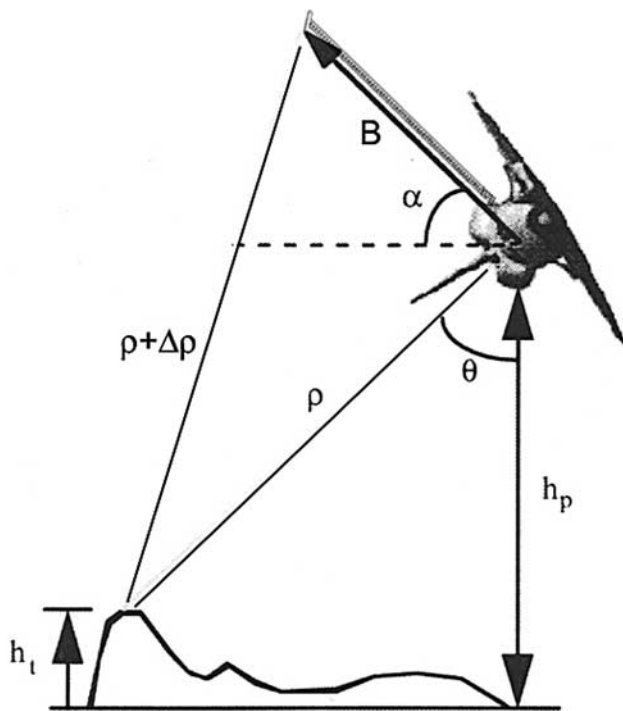


Figure 4. Geometry of the SRTM interferometer (not to scale). The mast formed the baseline B . Measurements of $\Delta\rho$, θ , α , B , and h_p lead to a solution for the height of the terrain h_t .

[19] A complexity involves the fact that only the path length difference is measured, and that is measured as an angular phase difference, which becomes ambiguous after a full cycle of 2π radians. Thus a method for finding the absolute phase and therefore actual path length difference is necessary [Madsen and Zebker, 1998]. This process is called phase unwrapping, and a number of algorithms have been invented to optimize the process [e.g., Goldstein et al., 1988]. Errors in phase unwrapping typically show up as elevation jumps of tens to hundreds of meters when estimates from one pixel to the next jump by 2π (the ambiguity height) or tilting caused by a poor choice of absolute phase.

[20] The size of the radar antenna limits the cross-track extent that can be illuminated by the radar. This ground swath was about 60 km wide for SIR-C and thus for SRTM. In order to meet the coverage requirements and complete a global map in 10 days a width of about 225 km was needed on each orbit of the mission. To increase the ground swath width by a factor of about 4, SRTM employed two techniques: (1) ScanSAR was used to roughly double the extent of the beam, and (2) to double the coverage again, signals with orthogonal polarizations were transmitted simultaneously, each with a different elevation steering angle (Figure 5).

[21] Reducing the illumination time for a target on the ground reduces the resolution; thus the swath is widened at the cost of azimuth resolution. For SRTM’s 12-m antenna transmitting at 5.6-cm wavelength (C band) and moving at a speed of 7.5 km/s at a range of 300 km, the target illumination time is roughly 0.2 s. Using only a portion of

this time, for example, a “burst” period of 0.05 s, to form a synthetic aperture reduces the resolution that can be achieved by a factor of 4.

[22] For SRTM, at least 50% of the synthetic aperture time was needed for adequate noise performance, allowing at most two electronically steered beams. As the intrinsic swath width was roughly 60 km, only 120 km could be covered by a single-polarization ScanSAR. To obtain adequate swath width, it was necessary to utilize the polarization capability of the SIR-C hardware. SIR-C could simultaneously transmit horizontal and vertical polarizations and electronically steer the horizontally polarized beam independently of the vertically polarized beam. In this way the horizontally polarized channel could be operated in ScanSAR mode covering two elevation swaths, and the vertically polarized channel could likewise be operated in two other elevations (Figure 5).

2. MISSION DESIGN

[23] SRTM was designed to meet a particular map accuracy specification. This stringent requirement, coupled with the characteristics of the existing SIR-C hardware, led to a constrained mission design space and a set of natural design choices for the mission. The goal of a radar interferometer is to measure the difference in range between two observations of a given ground point with sufficient accuracy to allow accurate topographic reconstruction. This is done through the interferometric phase and knowledge of the interferometer geometry (Figure 4). A simplified expression for the target height h_t is

$$h_t = h_p - \rho \cos \left[\sin^{-1} \left(\frac{\lambda\phi}{2\pi B} \right) + \alpha \right],$$

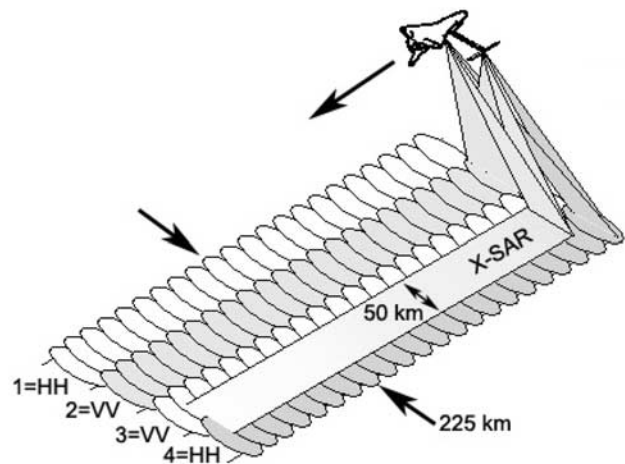


Figure 5. How the SRTM swaths were constructed. C radar illuminated a 225-km swath by alternately collecting pairs of subswaths using scanSAR. Subswaths 1 and 3 were illuminated first, then 2 and 4, etc. X-SAR was not able to scan, so its 50-km swath was fixed between subswaths 3 and 4.

where h_p is the platform height (antenna altitude with respect to the WGS84 reference ellipsoid [*Defense Mapping Agency*, 1997]), ρ is the range, ϕ is the measured interferometric phase, α is the baseline roll angle, λ is the observing wavelength, and B is the baseline length. Clearly, errors in knowledge of the quantities in this equation impact the total SRTM performance. The trade-off between these errors was a large part of the mission design. For SRTM the radar instrument provided data necessary to determine ρ and ϕ , while a metrology package (Attitude and Orbit Determination Avionics (AODA)), described in section 3.5, measured the detailed shape of the interferometer, in essence α , B , and h_p .

[24] The allocation of the vertical error to the various system components of SRTM was roughly as follows: phase noise, ~ 8 m; baseline angle, ~ 7 m; baseline length, ~ 1 m; platform location, ~ 1 m; and range ~ 1 m. The usual components of the radar equation, radar aperture size, radiated power, noise properties of the receiver, range to the target, and surface backscatter characteristics, were the given parameters of the mission, derived from SIR-C hardware and shuttle operations capabilities. These quantities set the intrinsic statistical phase noise performance of the interferometer. Given the phase noise of the system, the height acuity of the system can be controlled by the design of the remainder of the interferometer.

[25] The sensitivity of height to phase is given by the derivative of the above equation:

$$\frac{\partial h}{\partial \phi} = \frac{\lambda}{2\pi} \frac{\rho \sin \theta}{B \cos(\theta - \alpha)}.$$

Several terms in this equation were also established outside the design trade space. The choice of wavelength between L band and C band for SRTM was clear: An outboard C band antenna would have less mass and volume and was therefore obvious for a shuttle mission that was already pushing the limits of the vehicle's carrying capacity. The shuttle orbit of 233 km at 57° inclination was the highest possible for a fully loaded shuttle. Maximizing the altitude also maximizes the antenna footprint on the ground, contributing to achieving full circumferential coverage in 10 days of mapping. To minimize layover effects, look angles were chosen between 30° and 60° . These angles, along with the altitude, set the range extent of the swath. Thus in this sensitivity equation the only free parameters are the interferometric baseline B and orientation angle α .

[26] As the baseline becomes larger, the sensitivity of the height to phase noise is partially reduced. The phase noise is dependent on the backscatter properties of the surface: Poorly backscattering surfaces have lower SNR, with higher phase variance. It was important to characterize the anticipated worst-case backscatter at C band and choose the baseline length accordingly.

[27] The baseline angle was chosen to be 45° . This angle minimizes the sensitivity of the observation to errors in the baseline length. Given these constraints, B was chosen as large as necessary to meet the height noise requirement. For

a typical worst-case correlation of 0.7 and 2 looks, the phase noise is about 0.5 radians. The baseline length must be chosen so that after multiple observations are combined, the height noise is within the statistical height error allocation. For a baseline of 30 m, as was originally proposed, the statistical height noise (subject to the other interferometric constraints, as stated above) would be 25 m, an unacceptable magnitude. Even with two independent observations (ascending and descending orbits, for example) the statistical noise would be greater than the total height error budget of 16 m. It was determined that a 60-m baseline, yielding a worst-case statistical height noise of 12 m, was acceptable and would have to be accommodated in the payload design.

[28] In order to meet the statistical phase noise allocation of 8 m a key mission characteristic had to be at least double coverage of every point on the Earth. Thus the 12-m worst-case height noise could be reduced by a factor of $\sqrt{2}$ to about 8 m. Double coverage was achieved by observing every point on the ascending and the descending portion of the orbit. The orbit ground track separation at the equator was about 218 km; thus with a 225-km ScanSAR swath it was possible to just cover all points on the ground within the 10-day flight. Observations had to be made without failure on both ascending and descending orbits for points located within $\pm 20^\circ$ (latitude) of the equator. At higher latitudes, coverage overlapped as the orbits converged, but near the equator only one ascending and one descending pass was available.

[29] Another possible interferometric phase error can arise from relative phase differences between the two receiver channels. The receivers were not identical mechanically or thermally, and the signal path length from receiving antenna to electronics was vastly different because of the 60-m baseline. Rather than attempt to force the receiver phases to be identical, a calibration tone signal with common reference was distributed to the antennas over optical fiber cable to the deployed antenna [*McWatters et al.*, 2001]. The signals were injected into the receive paths at the antennas and detected in the data processing. The phase differences did indeed vary over the life of the mission by many degrees and would have been a significant error source had they not been compensated for in the processing. After compensation the error was less than 1 m.

[30] The next largest error source in the interferometer was the baseline angle, α . The sensitivity of height error to angle error is given by

$$\frac{\partial h}{\partial \alpha} = \rho \sin \theta,$$

which states that an error in baseline angle amounts to a height error ∂h given by the rotation of the ground range vector to the target ($\rho \sin \theta$) by angle $\partial \alpha$. To meet a height error allocation of 7 m, one must know the baseline angle to an accuracy of $7/233000$ or 3×10^{-5} radians (about 6 arc sec).

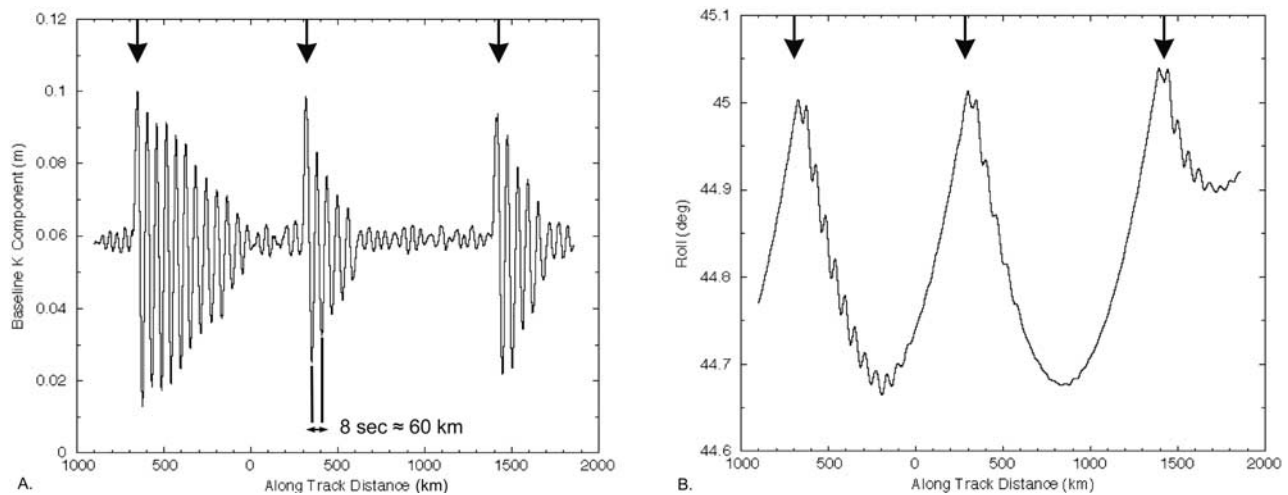


Figure 6. Mast motions induced by shuttle thruster firings (arrows) during data take 72.10 (flight day 4). (a) Displacement of mast tip as a function of along-track distance. Note maximum displacement of about 10 cm and the rapid damping. The fundamental period of the mast was about 8 s. (b) Shuttle roll angle as a function of along-track distance. Note gravity-gradient torque causing increase in roll angle between thruster firings. Shuttle dead band was approximately 0.3° .

[31] For a system where the baseline is slowly drifting, one can imagine a calibration scheme where any drifts in the baseline angle are removed by ground control points spread throughout the world. Indeed, the mission design stipulated that the data takes begin over the ocean prior to landfall and end over the ocean after mapping the land to deal with the possibility of long-term drifts. (It turned out that there was very little long-term drift.) However, as Figure 6 illustrates, the shuttle is a dynamic, mechanically oscillating system. Because thrusters were firing periodically to maintain the shuttle attitude, the mast resonated and oscillated. This resulted in a displacement of as much as 10 cm for the tip of the mast and a change of several tenths of degrees in the shuttle attitude. A few ground control points were therefore insufficient to determine the baseline. The metrology package (AODA) continuously measured the position and attitude of the shuttle and the outboard antennas to the required accuracy.

3. SRTM SYSTEM

3.1. SRTM Hardware and System Overview

[32] The SRTM architecture was based on the SRL SIR-C/X-SAR instruments, modified and augmented to enable single-pass interferometric operations. The resulting new system consisted of four principal subsystems: the C band synthetic aperture radar (C radar), the X band synthetic aperture radar (X radar), the antenna/mechanical system (AMS), and the AODA. Of the four major subsystems, C radar, X radar, and AMS utilized the well-tested SIR-C/X-SAR hardware. AODA was a newly developed subsystem. Substantial parts of AMS were also new. The unique concepts on which AODA was built and AMS was modified contributed substantially to the almost flawless execution of SRTM.

[33] Owing to its bulk and complexity the SRTM hardware took up all of the shuttle's cargo space (Figure 7). SRTM hardware was placed in the payload bay (Figure 8), in the middeck, and on the aft flight deck (AFD) (Figure 9). Hardware located in the AFD included three payload high-rate recorders (PHRRs), tape cassettes, digital data routing electronics (DDRE), recorder interface controller (RIC), and AODA processing computers (APC). The middeck hardware included two spare PHRRs, spare power supplies, spare computers and hard drives, spare cables, repair kits, and tape cassettes. A total of 350 cassettes were flown. A warm spare PHRR was carried in the middeck accommodation rack. The total mass of the SRTM payload was 13,600 kg.

3.2. C Radar Subsystem

[34] While much of the radar system was inherited from SIR-C, several new systems or modifications were necessary for interferometric operation: C band receive-only outboard antenna panels (supplied by the Ball Corporation), the beam autotracker (BAT) (Ball Corporation), and the calibration (CAL) optical receiver (COR). The elements of C radar located in the crew cabin were the DDRE unit, which multiplexed the high-rate data streams from C radar and X radar onto the PHRRs, under the control of the RIC (Figure 9). RIC was a laptop computer with software to handle all the faults and unusual recording situations that were encountered on SRTM. RIC received simple commands from the command timing and telemetry assembly, and it monitored the PHRRs to make sure that the commands were executed properly. It had an elegant new feature: the ability to calculate the moment when a data take would exceed the remaining tape capacity. It would then start up the second recorder in time for it to capture the data as the first recorder ran down. The overlap was such that the same data were recorded on both PHRRs for about

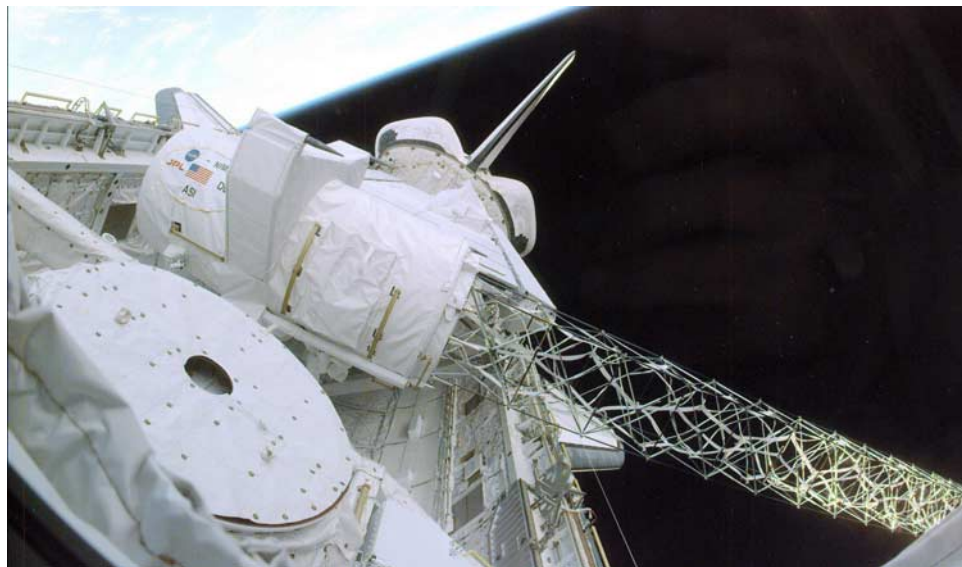


Figure 7. SRTM hardware in Endeavour's payload bay in mapping attitude. Nearest foreground is the space station docking adapter. Next is the mast canister with the partner logos. Note mast with many cables running its length. Main antenna is beyond canister. X-SAR antenna is on its right edge; C band antenna is at the left edge. The pyramidal object in the middle of the main antenna is AODA covered with thermal blankets. Johnson Space Center photograph s99e5476.

30 s. The astronauts were kept busy loading and unloading C radar tapes; the capacity of a single tape was 20 min at the C radar data rate. DDRE also had the ability to route real-time data or tape playback to the shuttle's Ku band signal

processor (KuSP). The KuSP was a link to JPL and the POCC via TDRS, the White Sands Ground Terminal, and DomSat.

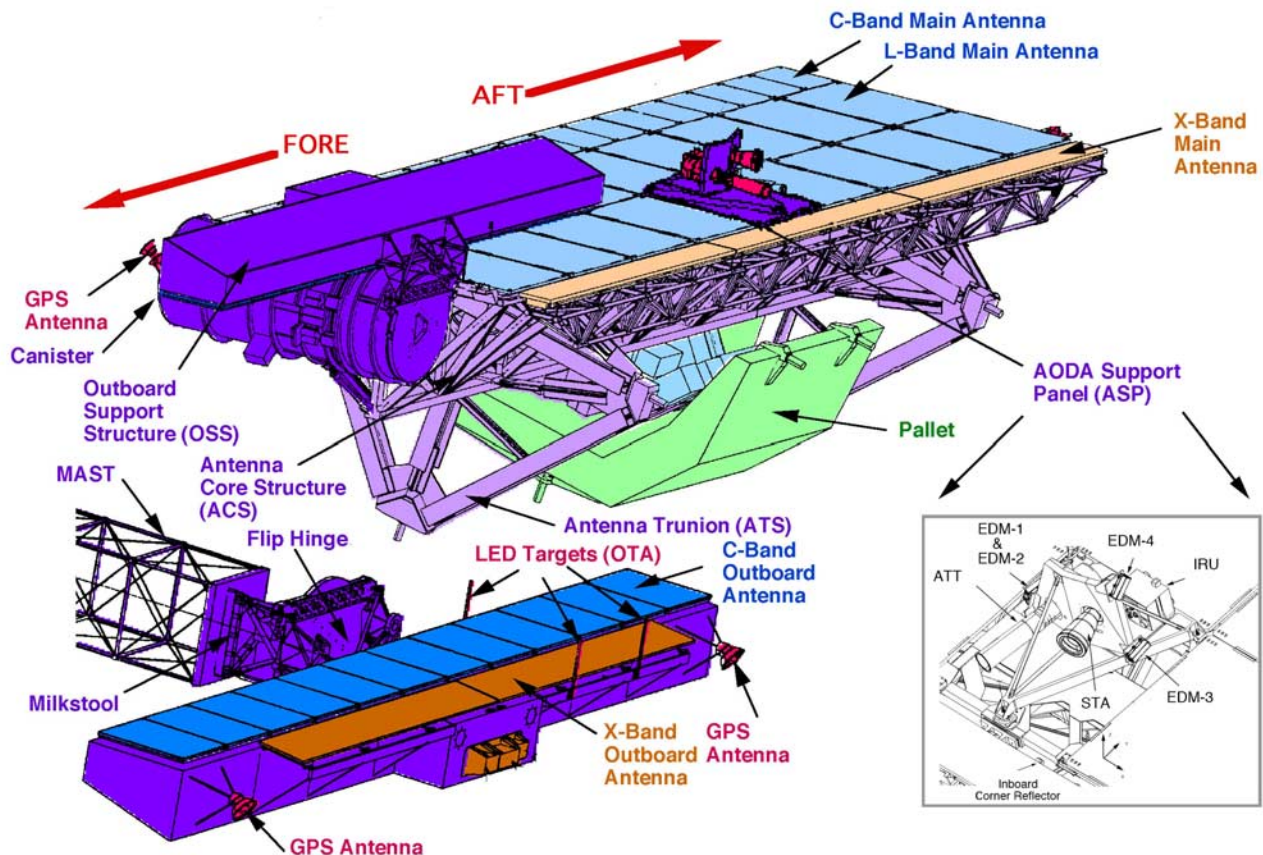


Figure 8. SRTM hardware in shuttle payload bay. (top) Stowed configuration. (bottom left) Deployed Outboard Antenna System. (bottom right) Details of the AODA support panel.



Figure 9. Mission Specialists Gerhard Thiele and Janet Kavandi go over the crew timeline in the shuttle aft flight deck. The laptop at top left is the recorder interface controller; its screen shows the status of three payload high-rate recorders (PHRR). Behind Thiele's arm are two PHRRs. Johnson Space Center photograph sts099_327_003.

[35] C radar incorporated an interesting design feature: the beam autotracker. The concept of BAT, first tested on JPL's airborne SAR (AIRSAR) test bed, seemed simple: Split the antenna into right and left beams, compare the signal strength in each, and then change the antenna pattern to equalize the signal strength. This electronic beam steering could compensate for rapid motions of the mast. The AIRSAR test showed that at least in some situations the concept worked. Fortunately, the mast proved to be quite stable over a data take, and thus BAT was not used.

3.3. X Radar Subsystem

[36] The 12-m-long and 40-cm-wide X band main transmit and receive antenna was mounted to the C band radar antenna truss structure in the shuttle cargo bay and mechanically tilted to -7° (59° off nadir), placing its 50-km beam between C radar beams 3 and 4 (Figure 5). The X-SAR main antenna and electronics were left nearly unmodified from the SRL missions. The new outboard receive antenna was only 6 m long, consisting of six 1-m panels (spare parts from SRL). It was mounted together with the X band outboard electronics to the outboard antenna support struc-

ture. On the backside of the six antenna panels, six low-noise amplifiers were attached, one for each panel. Together with the six controllable phase shifters, this enabled electronic beam steering of the outboard antenna within a range of $\pm 0.9^\circ$ in azimuth. The electronic pointing capability was designed for dynamic pointing based on the BAT signal to stay within the illuminated spot on the ground, but it was only used to correct for a slight static misalignment of 0.1° between the main and secondary antennas detected during OOCO.

3.4. Antenna/Mechanical System

[37] The SRTM mechanical system was based on the SIR-C/X-SAR system, with significant changes. The SIR-C/X-SAR instrument flew one row of 18 C band panels and two rows of 9 L band panels. SRTM retained the 18 C band panels and 6 of the L band panels, but since the L band system was not used, the superfluous panels were removed to save weight.

[38] The most significant SRTM hardware addition was the Outboard Antenna System (OASYS) and its deployment system. The OASYS consisted of outboard support struc-

ture (OSS), outboard C band panel array, outboard X band panels and electronics, and AODA equipment (Figure 8). The total weight of the OASYS was 397 kg. The OASYS deployment system included four major components: the 60-m mast and mast canister, a mast damping system, an OASYS flip hinge, and an OASYS static pitch and yaw attitude adjustment mechanism referred to as the “milk stool.”

[39] The mast, manufactured by AEC-Able Engineering, Inc., of Goleta, California, derived from the International Space Station solar array blanket support structure. The mast was a truss structure consisting of 86 bays plus the milk stool. Nominally, it took approximately 20 min to extend or retract the mast. The mast longerons and battens, longitudinal and transverse members, respectively, were pultruded graphite/epoxy rods. The mast diagonals were made of titanium wire rope. Four ribbon cables, two fiber optic cables, eight coaxial cables, and one nitrogen gas line ran the length of the mast (Figure 7). An orderly folding scheme assured that the cables stowed in a repeatable, compact shape. An extravehicular activity (space walk) to manually crank the mast if it failed to extract or retract was a part of the mission plan. The crew also had the option of jettisoning the canister/mast assembly. The mast canister was mounted to the forward end of the antenna core structure (ACS). In launch configuration the outboard antenna was folded across the top of the canister and the inboard antenna (Figure 8). The OASYS flip hinge rotated the OASYS 180° from its stowed position to its deployed position once the mast was deployed. The mast damping mechanisms were designed to achieve greater than 10% damping ratios in the first bending mode and the first torsional mode. The static OASYS pitch and yaw attitude was adjusted to align the outboard and inboard antennas via the milk stool during OOCO.

[40] The combination of the mast and the outboard antenna attached to the mast’s tip represented a momentum arm extending from the shuttle. The arm was not accounted for by the shuttle’s regular attitude control system. For mapping the mast had to point sideways, 45° relative to the nadir vector. The corresponding shuttle attitude would then be 59° from the bay-down orientation. The off-vertical pointing exposed the shuttle/mast system to a gravity-gradient torque. Anticipating this, a cold gas thrust system was added to OAS, with the purpose of providing a compensating torque. This was calculated to reduce the frequency of the shuttle’s thruster firings, thus conserving propellant. On flight day 2 it was determined that orbiter propellant usage had doubled from 0.07% to 0.15% an hour. The increase was caused by the failure of the cold gas thrust system due to a burst diaphragm.

[41] Correct pointing of the mast held the key to successful interferometric operations of the SRTM radars. Errors in pointing would lead to misalignment of inboard and outboard antennas and to the loss of interferometric capability. Apart from affecting the consumables budget the attitude control system firings had an additional consequence in that they triggered dynamic responses by the mast. Gravity

unloading, load shifts during the launch, and preflight assembly and alignment errors resulted in a quasi-static pointing bias. In-flight, thermal deformation of the mast and antenna structure created pointing errors with time constants of several minutes. (The mast’s primary modal frequency was on the order of 0.1 Hz.) Although the pointing challenges were mitigated by the SRTM structural and mechanical design, the mast pointing errors had to be measured continuously by AODA and compensated for by the radar instruments and the ground data processing system.

3.5. Attitude and Orbit Determination Avionics

[42] The primary function of the AODA system was to provide a postflight time history of the interferometric baseline for use in the topographic reconstruction processing [Duren et al., 1998]. For SRTM, AODA was required to provide estimation of the interferometric baseline length, attitude, and position to an accuracy of 2 mm, 9 arc sec, and 1 m (at 90%, or 1.6 sigma, confidence level), respectively. These requirements had to be satisfied throughout the entire mission whenever the radars were collecting data at a rate better than 0.25 Hz. During instrument development, however, AODA took on the additional requirement to support mission operations, including verification of in-flight mast deployment, antenna alignment, and shuttle attitude control optimization.

[43] Safety demanded that proper deployment of the mast be verified before the mapping phase of the mission. For instance, if one or more of the mast latches did not snap into place when the mast was extended, the structure might still have appeared unimpaired but would have collapsed when the shuttle thrusters fired. Endeavour remained in free drift in a stable gravity-gradient attitude during mast deployment and verification. AODA measurements of errors in the deployed mast tip position and attitude allowed the crew and ground teams to verify mast integrity before engaging shuttle’s attitude control system.

[44] The inboard and outboard antennas needed to be aligned in such a manner that the radar antenna beam patterns on the ground had maximum overlap. Roll misalignment was less critical because the beam width about the roll axis was relatively large, but errors about the pitch and yaw axes could not exceed 0.06° [Geudtner et al., 2002]. Following mast deployment, the astronaut crew used AODA measurements to guide static alignment adjustments in yaw and pitch utilizing the milk stool mechanism.

[45] Though preflight (1-g environment) estimates of mast modal frequencies were available, in-flight measurement was preferred. Since notch filter settings in the shuttle’s attitude control system could be selected to reduce mast response, errors in preflight estimates could result in inefficient on-orbit performance, i.e., excessive attitude control response and correspondingly excessive propellant use and mast motion. The consequence of nonoptimal propellant use could be a shortened mission. It turned out that this in-flight identification was crucial because the

passive damper at the root of the mast failed to function in flight.

[46] The AODA system consisted of a flight segment and a ground segment. The central part of the flight segment was the AODA support panel (ASP), kinematically mounted to the inboard ACS, in place of one of the removed L band panels (Figures 7 and 8). The ASP furnished an isothermal, optical-bench-type support for the following AODA sensors: star tracker assembly (STA), inertial reference unit (IRU), Advanced Stellar and Target Reference Optical Sensor (ASTROS) Target Tracker (ATT), and electronic distance meters (EDMs). With the exception of the STA this hardware consisted of inherited or commercial equipment in order to keep the cost low. AODA was necessary because the standard shuttle guidance and navigation system did not offer the required accuracy and because significant thermal distortions existed between the shuttle guidance platform and the SRTM inboard antenna.

[47] The baseline attitude had two primary components: the inertial platform or inboard antenna attitude and the (primarily) mast-induced relative motion between the two radar antennas. The inertial platform attitude was measured by STA and IRU. STA consisted of a Lockheed Martin autonomous star tracker (AST-201) instrument. The IRU was a Teledyne dry rotor inertial reference unit (DRIRU-II). The IRU measurements were useful in refining the attitude estimates during the postflight ground data processing. The ATT was critical for meeting four AODA requirements: baseline determination, antenna alignment, mast deployment verification, and mast modal identification. Developed by JPL in the 1980s as a high-precision star tracker for planetary missions, ASTROS required extensive modifications for use by SRTM. ATT tracked three red light-emitting diode (LED) targets (Optical Target Assembly (OTA)) located on the outboard antenna and separated by 1 m both laterally and in line of sight (Figure 8). AODA determined the outboard antenna's relative attitude and position based on the centroid information collected by ATT on all three OTA targets.

[48] Although the ATT provided good accuracy in determining 5 of the 6 outboard antenna degrees of freedom, it had degraded range accuracy because of OTA geometrical constraints imposed by the outboard antenna dimensions. Late in the AODA design phase it was deemed necessary to add an instrument capable of accurately measuring the baseline length, i.e., the range to the outboard antenna. A commercially available surveying rangefinder, Leica-Wild DI2002 EDM, satisfied the AODA requirements [Duren and Tubbs, 2000]. Four modified and flight-qualified units were utilized: two units to measure range to the outboard antenna and the other two units to measure displacements between the inboard C and X band arrays (each measuring one leg of a triangle to solve for X and Z displacement). The EDM outboard target was an array of cube corner-reflectors placed along the inboard edge of the outboard antenna. This arrangement allowed the two outboard-looking EDMs to acquire signal even in the event of large mast excursions. In

addition, a single cube corner reflector was placed on the inboard X band antenna.

[49] Orbit (platform position and velocity) determination was provided by an onboard GPS consisting of two P code tracking GPS Receivers (GPSRs) developed as part of JPL's TurboRogue Space Receiver Program [Duncan et al., 1998]. The onboard receiver position solution, via "direct GPS" technique, is limited to 10- to 100-m accuracy. To obtain the required 1-m position determination, the pseudorange and phase observables acquired by the onboard GPSRs were combined with those simultaneously available from the existing ground network of globally distributed, well-surveyed GPS receivers. Such an approach could be termed a "global differential GPS" technique [Bertiger et al., 2000].

[50] Two laptop computers with JPL-developed software served as the onboard AODA workstations (APCs). Located in the shuttle's aft flight deck (Figure 9), the APCs were heavily relied upon during OOCO. They fulfilled several functions, in particular, guiding antenna alignment and providing control loops for operating ATT and EDM. The AODA system was designed to operate and record autonomously once the mapping phase of the mission began.

[51] The AODA ground segment consisted of the global network of ground GPS receivers, the GPS Inferred Positioning System (GIPSY), the AODA Ground Data Processor (AGDP), and the AODA Telemetry Monitor/Analyzer (ATMA). The ground segment was used during the mission to support antenna alignment, mast modal identification, and quick-look height reconstruction. AGDP took the raw data from ATMA (or APCs, following postflight recovery), performed the attitude and baseline determination, recombined the GIPSY output data, and presented the radar processor ground segment with a single time-tagged data archive.

4. MISSION OPERATIONS

4.1. Orbit Maintenance

[52] In order to meet the mission requirements and to comply with shuttle operational constraints the orbit selected was circular, 57° inclined, with a mean altitude of 233.1 km. This orbit repeated the same ground track in 9.8 days after 159 revolutions. It produced ground tracks spaced at 218 km, measured orthogonal to the direction of travel, or at 252 km, measured along the equator. Since C radar had a mean swath width of 225 km, the nominal overlap was only 7 km. Pre-mission simulations had shown that orbit drift due to atmospheric drag would amount to about 1.5 km/d at the equator. Perturbations caused by drag on the 60-m mast and outboard antenna were difficult to quantify. Even so, it was evident that unless compensated for, the orbit drift would cause loss of swath overlap in about 24 hours. To prevent orbit decay, extremely precise control had to be designed into the mission. This control was exercised by a series of nonstandard orbit trim maneuvers, known as "fly cast" maneuvers, executed at a nominal frequency of one per day.

[53] The first of a series of “fly cast” maneuvers was performed on flight day 2. The fly cast maneuver was designed to reduce strain on the mast during the daily orbit boost maneuver. The shuttle, which flew tail first during mapping operations, was moved to a nose-first attitude with mast extending outward. A brief pulse began the maneuver. The mast deflected backward, and when it reached maximum deflection, the main burn was performed, pinning the mast. After the burn the mast returned forward. As it reached the vertical, another pulse was applied, arresting the mast’s motion.

[54] The failure of the cold gas thruster at the tip of the mast constituted the most significant obstacle in flight. Without the thruster’s counteraction of gravity gradient torques on the orbiter plus mast the shuttle used up much more propellant than planned for attitude control, reducing the amount of propellant available for orbit maintenance. In order to complete mapping with the reduced amount of propellant, shuttle navigators and the SRTM mission planners worked out a new maneuver sequence for orbit trim burns 6–9. Trim burns 8 and 9 were deleted, the Δv of trim 6 and 7 was increased, and trim 7 was postponed by about 12 hours. The operations team selected a phasing and choice of Δv that were creative enough to cause no gaps to open up between radar swaths. Therefore it was possible to successfully complete mapping operations without significantly impacting the end results.

4.2. Ground Operations

[55] The complexities involved in securing proper interferometric performance on the part of the SRTM radars required participation by both the astronaut crew and dedicated ground teams. The crew controlled pallet and antenna activation and deactivation, initial antenna alignment, and tape change outs. The SRTM ground teams, located at the Payload Operations Control Center at NASA’s Johnson Space Center (JSC), the Customer Support Room at JSC, and the Mission Support Area (MSA) at JPL, controlled the rest of the SRTM activities. Each of the two SRTM radars was operated by a separate system centered at the POCC. Operations of C radar were handled by the Mission Operations System (MOS), and those of X radar were handled by the Mission Planning and Operations System (MPOS). The JPL MSA, networked to the POCC, was responsible for processing C radar data down linked from the shuttle during the mission. DLR had a similar system set up in Germany. The down link connection to JPL was routed through the NASA Tracking and Data Relay Satellite System and the White Sands Ground Terminal, while a separate high-rate data link was used to transmit processed images and measurements to JSC.

[56] Characterized in the most general terms, the operating systems for C radar and X radar performed parallel and equal tasks: mission planning, instrument commanding, instrument health monitoring, and instrument and system performance analysis. A brief description of MOS as the representative of both systems should thus suffice. Referring to Figure 10, note that MOS consisted of six major

subsystems: Mission Planning Subsystem (MPS), Command Management Subsystem (CMS), Telemetry Management Subsystem (TMS), Performance Evaluation Subsystem (PES), Data Management Subsystem (DMS), and ATMA. The Mission Planning Subsystem generated orbit predictions, performed SRTM long- and short-term planning, and produced mission timelines and C radar command inputs. Generation of ephemerides was done utilizing the Orbiter state vectors received from the Mission Control Center (MCC) every 2–3 orbits. Using these, MPS planned the start and stop times of each data take. Further, using a low-resolution DEM, it computed the distance to the surface of the Earth during mapping. By knowing this distance, MPS could select the appropriate set of radar parameters. The C radar mission timeline was produced every 6 hours and was sent to MPOS with the goal of generating X radar timelines and commands. MPS then added PHRR playbacks and other C radar and X radar events to the data take timeline. The finished mission timeline was provided to the MCC planners for crew flight plan inputs; it was also forwarded to the SRTM Customer Support Room and to the JPL MSA.

[57] On the basis of the mission timeline, MPS generated the C radar command input file. Using the command input files produced by MPS, the CMS generated time-tagged commands for uplink to C radar. CMS also had the capability to generate immediate (real time) commands. In addition, CMS received AODA block commands and formatted them for uplink to the AODA flight instruments. The TMS could be viewed as the CMS downlink counterpart. TMS decommutated the Orbiter operational downlink telemetry and split it into the C radar, AODA, Orbiter instrumentation, and Orbiter Systems Management data streams. The all-important AODA stream was routed to the ATMA in the POCC. Commands were sent to the onboard instruments via MCC and the S band link to the orbiter subsystems. Instrument telemetry was received over the same link. Last, the PES evaluated the single-channel and double-channel (interferometric) performance of the C radar instrument during the mission and, in conjunction with MPS, provided orbit-by-orbit reports of those data takes that failed to meet the mission requirements. PES also monitored beam alignment as measured by the AODA instruments, the (unused) C radar BAT, the JPL Radar Verification System (RVS) at the JPL MSA, and the echo profile information from both C radar and X radar. PES coordinated inboard/outboard antenna adjustments using the milk stool, and it performed steering of the inboard and outboard antennas. PES tools were used to predict echo strength, thermal noise, range and azimuth ambiguity levels, and relative height error and to monitor gain settings, swath overlap, and BAT alignment. The accuracy and stability of the alignment and the mast dynamics experienced throughout the mission was less than 0.025° and was better than expected. No dynamic steering of the secondary antenna beam with the BAT was necessary.

[58] At calibration sites in southern California, northwestern Australia, and near Munich, Germany, radar corner

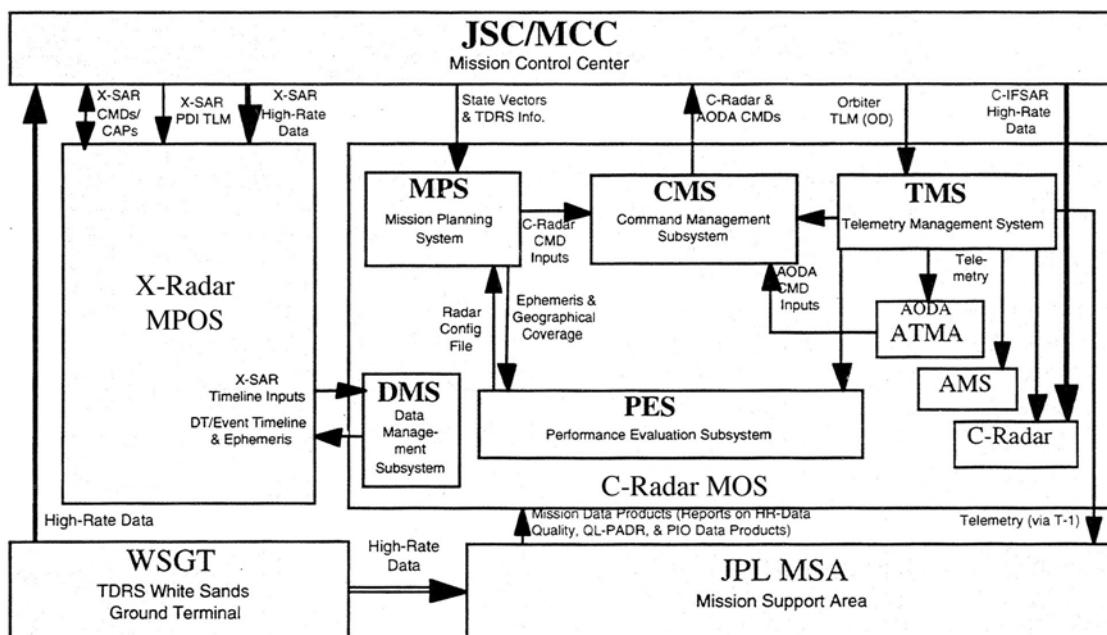


Figure 10. SRTM Mission Operations System. Johnson Space Center (JSC) Mission Control Center was the main interface to the shuttle for C radar Mission Operations System and X radar Mission Planning and Operations System in the Payload Operations and Control Center (POCC) at JSC (central part of diagram). JPL Mission Support Area processed C radar data and returned results to POCC via tracking and data relay system.

reflectors were deployed, and ground truth data were acquired. The alignment between the C band and X band radar systems was verified, and the azimuth antenna patterns were measured with radar receivers during the passes over the German calibration site.

[59] During the SRTM mapping phase of 222.4 hours, C radar operated for 99.2 hours, and X radar operated for 90.6 hours. A total of 765 data takes were executed. Of these, 399 were C radar only, 1 was X radar only, and 365 were simultaneous C and X radar. Classified by their purpose, 674 data takes were over land, 30 calibration data takes were over ocean, and 61 data takes were dedicated to equipment testing. The number of high-density tapes used was 330 (208 for C radar data, 122 for X radar data). The volume of data produced by SRTM, 12.3 Tb (8.6 Tb by C radar, 3.7 Tb by X radar), compares to the capacity of the Library of Congress.

[60] After Endeavour landed at KSC, the flight tapes were unloaded and formally handed over to the C radar and X radar ground processing teams. Over the subsequent 8 weeks the tapes remained at KSC while teams separated and transcribed the raw C and X band data to secondary sets of tapes. These secondary tapes were the ones that were eventually used for DEM processing, while the flight tapes were shipped to a secure archival facility for safekeeping.

4.3. Real-Time Analysis

[61] The data down linked during the mission were processed as soon as they were received, allowing a near real-time look at the quality of the data and a chance for new

discoveries. Real-time down links would only accommodate one channel, so no real-time tests of the full interferometric capability were possible. However, tape playbacks at reduced speed allowed full interferometric processing to DEMs for both the C and X band systems. It was apparent immediately that in those parts of the world where high-quality cartographic coverage was sparse the SRTM data brought a vast improvement. This bolstered confidence in the performance of the SRTM engineering systems and demonstrated the value of the rapid processing of the down linked data. By the time the Endeavour flight ended, mission personnel knew that a new topographic data set of great depth and richness had been acquired.

5. DATA PROCESSING

[62] Except for early comparative analysis of performance for the purpose of fine tuning the AODA solutions the C radar and X radar data were processed independently. The processing systems, developed on either side of the Atlantic, shared many general characteristics, but the details of the algorithms and implementations varied greatly. For example, the multibeam ScanSAR interferometric approach that C radar needed to cover the globe required a specialized burst-mode processor [Holzner and Bamler, 2002]. The X radar acquired data in a single beam in a continuous strip at the expense of limited coverage. Other differences arising from the coverage issues are described below.

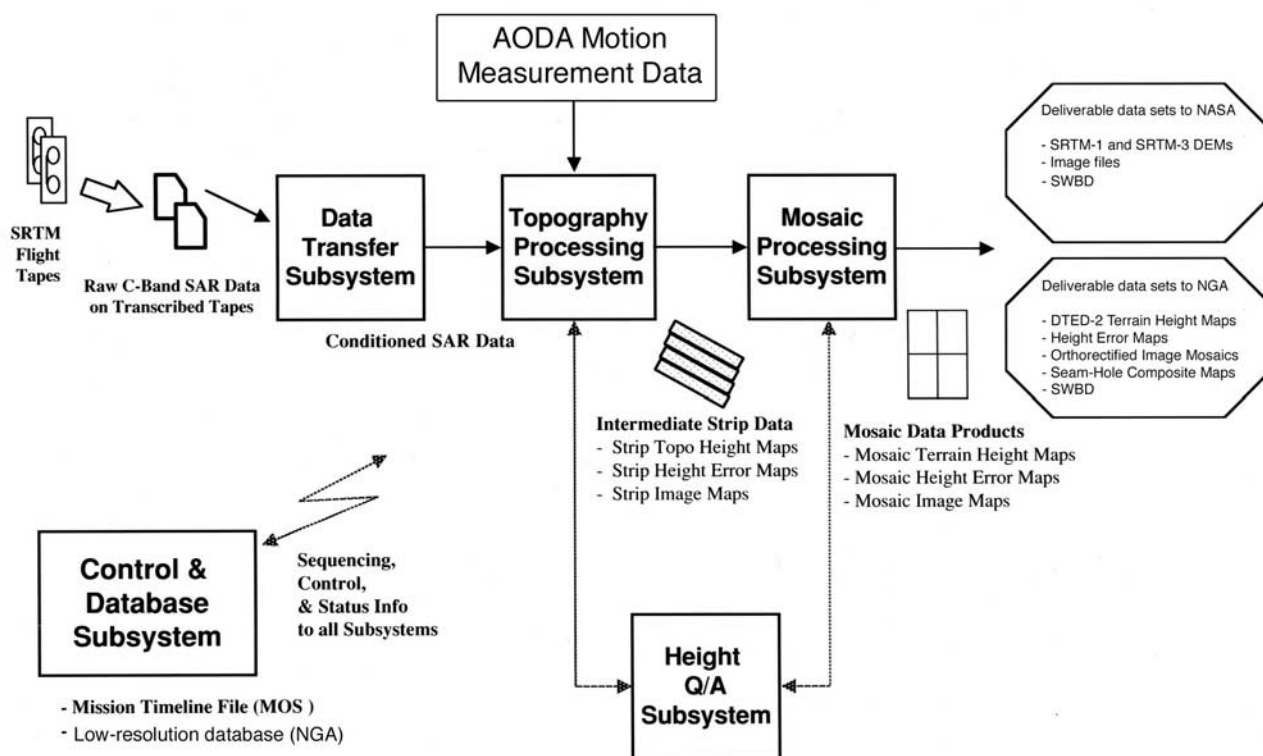


Figure 11. SRTM processor. Three main subsystems processed SRTM data to DEMs: data transfer, topography processor, and mosaicker. Calibration and validation (Q/A) contributed to several parts of the processor.

5.1. C Radar Algorithms

[63] The approach to reducing nearly one trillion paired pulse echoes of radar data to a continentally seamless digital elevation model, accurate to about two parts in 10^5 , involved reliance upon years of experience in the development of radar interferometry algorithms for airborne and spaceborne topographic mapping applications. Some of the SRTM algorithms were simple adaptations to the space environment of airborne single-pass approaches. Others required significant rework and innovation. Figure 11 shows the overall algorithmic flow for C radar processing. Motion and telemetry data were resampled to a uniform grid that was tailored to each data take and latitude band. The preprocessed data were then processed to elevation data mapped to a locally spherical coordinate system. The freshly processed data were immediately checked for quality against existing topographic databases. Passing that test, they were entered into an archive as the data takes for a continent were accumulated. When all the data take processing was completed for a continent, the data were further manipulated and adjusted to produce a seamless, self-consistent equiangular elevation model for the continent. The model was tied down at the coasts by well-known ocean heights corrected for tidal effects. The continental data were validated, error statistics generated, and then segmented into $1^\circ \times 1^\circ$ cells for distribution.

5.1.1. AODA Processing

[64] As described in section 3.5, the AODA system and data were a key aspect of the interferometer. Reduction of

the data to give position and velocity of the shuttle and a time-varying baseline vector involved the blending of data from systems with different time bases, sampling rates, and latencies. Very small errors in sampling or delay could cause large errors in the final height map; these errors were not easily removed because biases were not fixed. This is both a curse and blessing: Uncompensated errors could be large, but given the large amount of reference ocean data, it was fairly straightforward to sort out errors.

[65] AODA data reduction algorithms were extensions of well-established navigation solutions developed at JPL for deep space missions. While planetary spacecraft rarely experience the dynamic environment of the shuttle, a Kalman filtering approach was easily tailored to it [Wong *et al.*, 2001; Duren *et al.*, 1998]. Instrumental effects in the cameras, saturation of the LEDs, blinding of the star cameras due to shuttle wastewater dumps, etc., required prefiltering of the data, including some editing by hand.

[66] GPS processing using GIPSY was carried out on overlapping orbit arcs. Self-consistency of the solutions was checked in the overlap regions, and agreement to better than 1 m was found in general.

5.1.2. Low-Resolution and Calibration/Validation Databases

[67] The assembly of databases that could be used to aid the processing and serve as the calibration and validation points was an important component of preparation for the processing. A full report on SRTM calibration and valida-

tion has been presented by *Rodriguez et al.* [2005], and a condensed version is available [*Rodriguez et al.*, 2006]. This activity spanned nearly the entire period of instrument development; it involved active coordination with NGA and their international partner agencies for data sharing and new ground truth acquisitions. In particular, the following data sets were assembled:

[68] 1. A global digital elevation model, composed of the best digital elevation data available up to Digital Terrain Elevation Data (DTED-1) was generated with a 500-m post spacing. The purpose of these data was to aid the topographic processor in deciding what the approximate local height actually was and as a first check of topographic quality of the processor product. Tidally variable ocean heights formed an important part of the initialization of the data take processing. Since ocean heights varied over the duration of the mission, a static DEM was of little use. Instead, for each data take a tailored DEM was generated consisting of the static heights over land and tidally adjusted TOPEX/Poseidon-derived ocean heights.

[69] 2. Ground control points were derived from NGA historical data, offering accurate heights at several thousand points (specified by their latitudes and longitudes) around the world. These points could be used in either calibration of the data or validation of the final product (but not both).

[70] 3. Kinematic GPS data were acquired by driving an appropriately equipped GPS receiver across nearly every continent, north to south and east to west. The goal was to provide validation data and characterization of the spatial spectrum of height errors in the data.

5.1.3. Time-Varying Parameter Files

[71] The Earth's surface was divided into latitude bands where, for geometric convenience, the ellipsoidal shape of the Earth could be well approximated by a sphere. A complete data take would extend from ocean to ocean and would be divided into as many latitudinally controlled segments, called peg regions, as required. A peg region was defined by a single latitude, longitude, and heading known as the peg point, from which the coordinate transformation (and its inverse) from a spherical radar mapping coordinate system to the cartographic system is described analytically [*Madsen and Zebker*, 1998]. The output topographic map (as well as radar brightness and statistical error image products) was represented in this spherical system.

[72] Time is usually the independent variable against which other sensor quantities are characterized. However, once the geometry of the peg region was established, it became more convenient to describe the position along the spherical arc in the local coordinate system as the independent variable. This position is related to time through the spacecraft velocity, but a uniform time grid does not necessarily lead to a uniform spatial grid since the velocity may change with time. All parameters needed for tying the radar pulse data to the parameters of the instrument, including time, cross-track position, velocity, interferometric baseline, and radar mode changes (among others), were resampled in order to be placed on this uniform spatial grid. This approach greatly simplified the algorithmic logistics.

The grid was spaced at precisely 20 m, matched to the intrinsic along-track resolution obtainable from each burst.

5.1.4. Topographic Processing of Radar Data

[73] With the availability of the preprocessed motion and auxiliary radar mode data and low-resolution databases, it was possible to develop a processor that began processing at the beginning of a data take, typically over ocean, and ended at the end of a data take. Furthermore, the processor software was written to allow continuous processing through a data take, even if the data take spanned more than one peg region. Special algorithms were included to overlap the processing from one peg region to the next and to pass height values in the overlap region from one peg region to the next. This allowed bootstrapping (see below, in the discussion of phase unwrapping) of the height, minimizing the reliance on often faulty low-resolution databases for the reference height information.

[74] The hierarchy of topographic processing is illustrated in Figure 12. A collection of pulses composed a burst, and each burst was processed to an image tile that was roughly 1 km along track and 60 km across track. The processing also included a traditional range motion compensation algorithm to reference the motion of the inboard and outboard antennas to a common reference track. While motion compensation was not strictly necessary from an image quality perspective (motion within a synthetic aperture was well below a resolution cell dimension), it greatly simplified the processing farther downstream. Also, intermediate interferometric data products showed only topographic phase effects not mast motion effects.

[75] As a result of motion compensation, image tile pairs from the inboard and outboard antennas were aligned point by point in range and along-track position and directly combined to form burst interferograms. A collection of bursts was processed as a group to form a "patch," having a common grid and phase reference, so the burst interferograms could be laid onto a patch grid directly by accumulation. Adjacent bursts in the worst case overlapped each other by 50%. Thus each patch interferogram was composed of data with at least two radar looks per pixel and often more. It was important to keep track of the number of looks in a given pixel to calculate the height noise from the correlation.

[76] The phase of each patch interferogram was then unwrapped using a connected component variant of the standard branch-cut algorithm [*Goldstein et al.*, 1988]. After extensive testing of all known phase unwrapping algorithms such as least squares, minimum cost flow, and branch-cut variants on simulated SRTM data, it was determined that there was no significant advantage to using anything more complicated or computationally expensive than branch-cut methods. For production the property of branch-cut methods that is typically viewed as unfavorable, that is, incomplete area coverage, is actually a desirable conservative property. This is particularly so when coupled with connected component logic where, within the patch, large contiguous blocks of phase are tagged individually as unwrapped and can be compared to the low-resolution

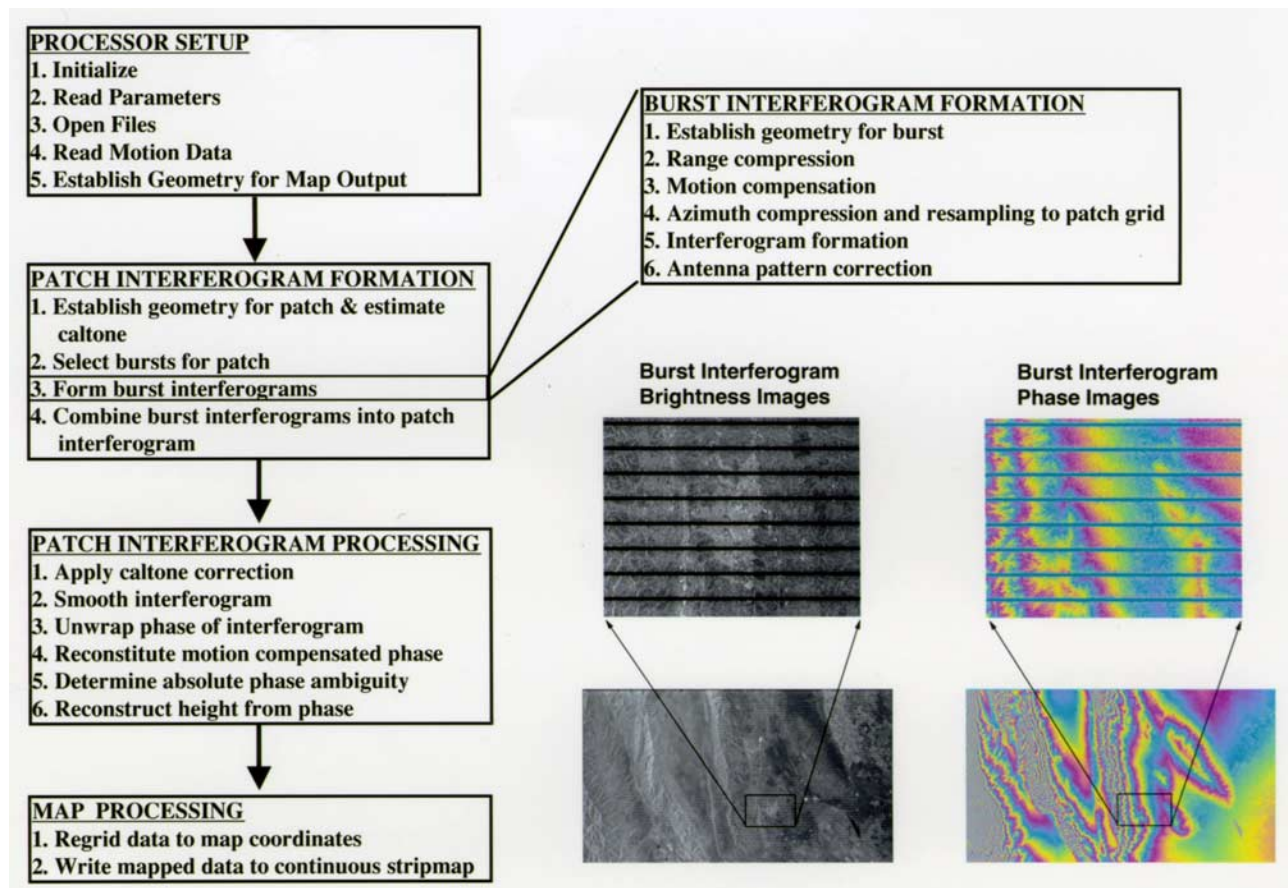


Figure 12. Topography processor subsystem. The processor starts with raw radar data and AODA motion data and produces strip maps and image data.

database to determine the proper phase ambiguity [Rosen *et al.*, 2000]. Thus layover, shadow, and decorrelation are not impediments to large area phase unwrapping, and ascending/descending cross checks in combination with the low-resolution database can assure an accurate result. Even so, a number of phase unwrapping errors were subsequently discovered in the SRTM DEM. These typically take the form of a sudden jump in elevation approximately equal to a multiple of the ambiguity height, which ranged from about 125 to 325 m. An example discovered by a user is Mount Roraima in Venezuela (J. de Ferranti, personal communication, 2004), which is a plateau surrounded by sheer rock cliffs over 400 m high. The plateau is nearly surrounded by void values, but elevations were found for the plateau itself. These values, however, are about 400 m too low. NGA has initiated a search for unwrapping errors in the SRTM data set [Ham, 2005].

[77] Once unwrapped, the phase is restored to its original variability before motion compensation to ensure consistency with the true physical baseline in the height reconstruction equations. The collections of (range, azimuth, and phase) triplets in the patch are then mapped one by one to spherical coordinate triplets in the height reconstruction process. These triplets are not uniformly spaced on the spherical output grid; this is accomplished by a regridding step.

[78] Regridding for SRTM was done in a way that allowed for adaptive variable-resolution smoothing. The intrinsic resolution of the SRTM interferometric products with no smoothing was very close to 30 m, but a product generated at this resolution would have point-to-point statistical height error that, while within requirements, would not be pleasing or useful to many users. It was decided that in flatter areas it would be best to degrade the resolution to smooth out this noise. An algorithm was devised to compare a computed statistical noise estimate to a theoretical value based on the interferometric correlation. If the computed noise exceeded the theoretical expectation, it was regarded as a highly variable region of terrain and less smoothing was done. Flatter, smoother regions were smoothed more. The final product resolution varies typically from 45 to 60 m [Smith and Sandwell, 2003]. The regridding method was based on a variable width weighted convolutional interpolation kernel. Since the data are not uniformly spaced going into the regrider, it would not be possible to achieve good performance by laying down the data to the grid with no smoothing and then smoothing later.

[79] Each patch was mapped to a master output grid for the entire peg region. When the peg region was complete, the processor moved on to the next region seamlessly until the data take was completed. All ascending and descending data takes within a continent were processed and checked

for quality and consistency before proceeding to the merging of data into a continental product.

5.1.5. Calibration Efforts

[80] Geometric and phase calibration of the interferometer was an essential part of processing the data. Since many components of the system, the baseline and receiver phase characteristics in particular, varied over time, these quantities could not be calibrated per se. Therefore the calibration strategy employed was to determine those quantities that were stable over the 10 days of the mission and estimate them statically and then dynamically estimate those that varied with time.

5.1.5.1. Radar Range Calibration

[81] Knowledge of the time delay for the inboard radar determined the absolute range accuracy of the product. The range delay was determined to be constant to the accuracy of a few meters by comparing the range to corner reflectors as measured in the radar slant range images to that derived from knowledge of the corner reflector locations and the position of the shuttle, both accurate to better than 1 m. Corner reflectors were deployed and surveyed for this purpose over areas in California and Australia.

5.1.5.2. Phase Screen Calibration

[82] The antenna pattern of the inboard and outboard antennas was different in both amplitude and phase, and because the antennas were beam-spoiled phased arrays these pattern characteristics were different for each antenna for each electronic steering direction. As a consequence it was important to measure the intrinsic antenna phase difference across elevation angles between the two antennas at each electronic beam position in order to compensate for this difference. This calibration vector is called the elevation phase screen.

[83] A sensible place to measure the phase screen is over the ocean, where the surface height is nominally zero relative to the local geoid. Any nonzero height measured across the swath in elevation could be attributed to the phase screen. By estimating phase screens over the 10 days of the mission and at numerous locations globally, it was determined that the phase screens were stable and constant. A single set of phase screens for all beam positions sufficed for the mission.

5.1.5.3. Dynamic and Ocean-to-Ocean Calibration

[84] There was some question whether the horizontal and vertical polarization channels that were used to form the two pairs of subswaths of the SRTM swath (Figure 5) would have a time-dependent phase difference. While phase screens could correct the error across any given subswath, drift of a phase screen relative to that of another channel would lead to height discontinuities across the swaths. An active part of the calibration and quality assessment phase was to compare heights between the subswaths and determine their difference, mapping this to a subswath-to-subswath phase difference. Three subswaths could then be corrected relative to a fourth. The overall phase drift of the fourth subswath was corrected by examining the height of the ocean at each end of a continental pass. Height differences from the geoid were attributed to phase drift in

that subswath, and a linear phase fit correction was calculated to detrend the pass. Refinement of this drift component at the peg region level was accomplished in the bundle adjustment phase described below.

[85] The static corrections, range delay and phase screens, were applied in the production of the strip data. The dynamic corrections were estimated on a pass-by-pass basis for a continent and applied as corrections in the mosaicker.

5.1.6. Continental Mosaicking

[86] One of the important distinguishing features of the SRTM mission relative to other large-scale mapping efforts is that the data set is intrinsically three-dimensional and self-consistent geometrically over the globe. This feature considerably improved the ability to mosaic the data. The purpose of mosaicking is to create a single, synoptic data product from a number of smaller products. Typically, a mosaicked DEM is composed of smaller DEM tiles that overlap on one or two edges of the individual tiles. To mosaic the DEMs, offsets and scale factors are estimated to force consistency of all tiles, and often an arbitrary mathematical transformation is used for this purpose. Without adequate tie points from one tile to the next or ground control points these kinds of weakly constrained “bundle adjustments” can lead to distortions in the final DEM. For SRTM the high degree of interwoven overlap of the ascending and descending data was a critical feature in assuring data quality and consistency, allowing the mosaicking process to be performed over an entire continent without concern for large-scale distortion.

[87] In principle, and with perfect calibration, the peg-based topographic data described above could be laid down on an output grid with only a well-defined transformation from peg coordinates to the output grid coordinates, thus eliminating the need for a bundle adjustment of data. While the above-described calibration efforts demonstrated very good stability and gave confidence in the performance, it was difficult to validate on a continental scale. Therefore a procedure to generate a continental set of tie points and ground control points was devised. From these, self-consistency could be checked over all scales, and adjustments could be made as necessary.

[88] Tie points were generated from the overlapping ascending/descending strip data sets and from adjacent overlapping swaths on either ascending or descending passes by cross-correlating either image brightness or topographic relief and detecting any offset between the two. Radar brightness is highly dependent on the observing direction, so most of the tie points were generated from cross-correlation of topography. These estimates were accumulated for an entire continent and used to adjust all strips relative to the others. The cross-correlation procedure produces formal covariance estimates that are propagated into the bundle adjustment as errors on the estimate.

[89] Ground control points were provided by NGA from a global database. The control was considered to be not photoidentifiable, so the control was used in the bundle adjustment as a constraint on a particular latitude-longitude

pair. Not all these points were delivered with formal errors, and many of the points were not as accurate as originally believed.

[90] The height error was characterized with a simple model:

$$\partial h = \frac{\partial h}{\partial \phi} \Delta \phi + \frac{\partial h}{\partial B} \Delta B + \frac{\partial h}{\partial s} \Delta s + \Delta H,$$

where ∂h is the height error and $\Delta \phi$, ΔB , Δs , and ΔH , are errors in the phase, baseline length, along-track position, and platform height, respectively. By assuming that these errors were quadratic functions of s alone, e.g.,

$$\Delta H = H_0 + H_1 s + H_2 s^2,$$

it is possible to estimate a suite of coefficients for the corrections to these errors for each peg-based swath in a continent by minimizing the difference between strips and ground control and strip-to-strip tie-pointed height differences in a grand least squares inversion.

[91] The Earth was divided into five “continents” and five island groups (Figure 13). Parameters were estimated en masse for an entire continent or island group. Note that the baseline angle error was not estimated because it is highly correlated with the phase error and could not be distinguished at this level of accuracy.

[92] Because calibration of the interferometer was stable and each individual strip nearly met its specification, it was only necessary to estimate an along-track positional shift Δs and overall sensor phase shift $\Delta \phi$ appropriate for all four subswaths of a data take over each peg region. As many as 40,000 parameters might be estimated for a large continent simultaneously. Residuals were examined, and the fits were adjusted if necessary to remove outliers. Parameter estimation took roughly 1 week of iteration per continent to optimize the solution. In the process of improving the fit it turned out that much of the preexisting ground control, claimed to be accurate at a sufficient level of accuracy for the purpose at hand, contained substantial elevation errors, enough to throw off the fits. After some iterations much of the ground control was discarded, and ultimately, the improvement of the data sets relied most heavily on the self-generated tie points between overlapping data takes.

[93] Once the corrections were estimated for each continent, the strip data could be assembled into a final mosaicked digital elevation model. For each output cell all relevant strip data were identified. For each output pixel in the cell, data from each strip were assembled and adjusted in three-dimensional position according to the corrections determined above. These corrected data were interpolated to the output grid. All height data were combined with error weighting and feathering as

$$\hat{h} = \frac{\sum_{i=1}^{N_h} h_i w_i}{\sum_{i=1}^{N_h} \frac{w_i}{\sigma_{h_i}^2}},$$

Where N_h is the number of height measurements, w_i is a spatially variable weighting that allows a smooth transition in regions of overlap and $\sigma_{h_i}^2$ is the variance of the height error as determined from the interferometric correlation. It was smoothed relative to the height itself to reduce noise in the error estimate.

[94] Finally, the heights were converted to the EGM96 geoid [Lemoine et al., 1998] using a full 360×360 harmonic expansion evaluated at $1/10^\circ$ intervals and a bilinear interpolation. The heights were then quantized to 1 m.

5.1.7. SRTM Validation

[95] SRTM data products were validated on continental scales through comparison with reserved ground control (i.e., control not used in the mosaicking bundle adjustments). The best quality control data were the kinematic GPS data acquired by JPL and NGA specifically for SRTM validation. Long tracks of GPS estimates were acquired along roads on most major continents. These data were accurate to better than 1 m and could characterize SRTM errors on spatial scales from hundreds of meters up to thousands of kilometers. With these data it was possible to develop a spatial error spectrum and total absolute error estimates that have high confidence and are generally applicable away from the kinematic tracks themselves.

[96] Table 1 summarizes the 90% errors estimated using the available ground truth [Rodriguez et al., 2005, 2006]. The absolute vertical accuracy is better than 9 m, indicating that SRTM improved on its design goal of 16 m absolute by almost a factor of 2. Figure 14 shows the spatial patterns of the vertical error. Note that the greatest errors are associated with steep terrain (Himalayas and Andes) and very smooth sandy surfaces with low SNR (Sahara Desert).

[97] The remaining SRTM error can be thought of as consisting of three parts: First, there is a long-wavelength component, due to residual roll errors, with a magnitude of about 2 m and a spatially nonstationary behavior. The second component consists of random (i.e., medium to short wavelength) errors which add an additional spatially varying error component. Finally, at the shortest scales, speckle noise decorrelates for separations on the order of one to two pixels.

[98] Combined with the adaptive filtering carried out during the regidding step, speckle noise affects slope measurements made with SRTM DEMs. Speckle has the effect of increasing slope estimates at short scales, while the smoothing step decreases larger-scale slopes. This effect has been noted by several users of SRTM data [e.g., Alsdorf et al., 2007; Kiel et al., 2006; Guth, 2006; Falorni et al., 2005].

[99] Areas of extreme errors or from which no radar signal returned were given a void value of -32768 . Voids were caused by two main mechanisms: steep slopes facing away from the radar (shadowing) or toward the radar (foreshortening or layover) and smooth areas such as smooth water or sand which scattered too little energy back to the radar to create an image [Hall et al., 2005]. As many applications require a continuous DEM with no voids,

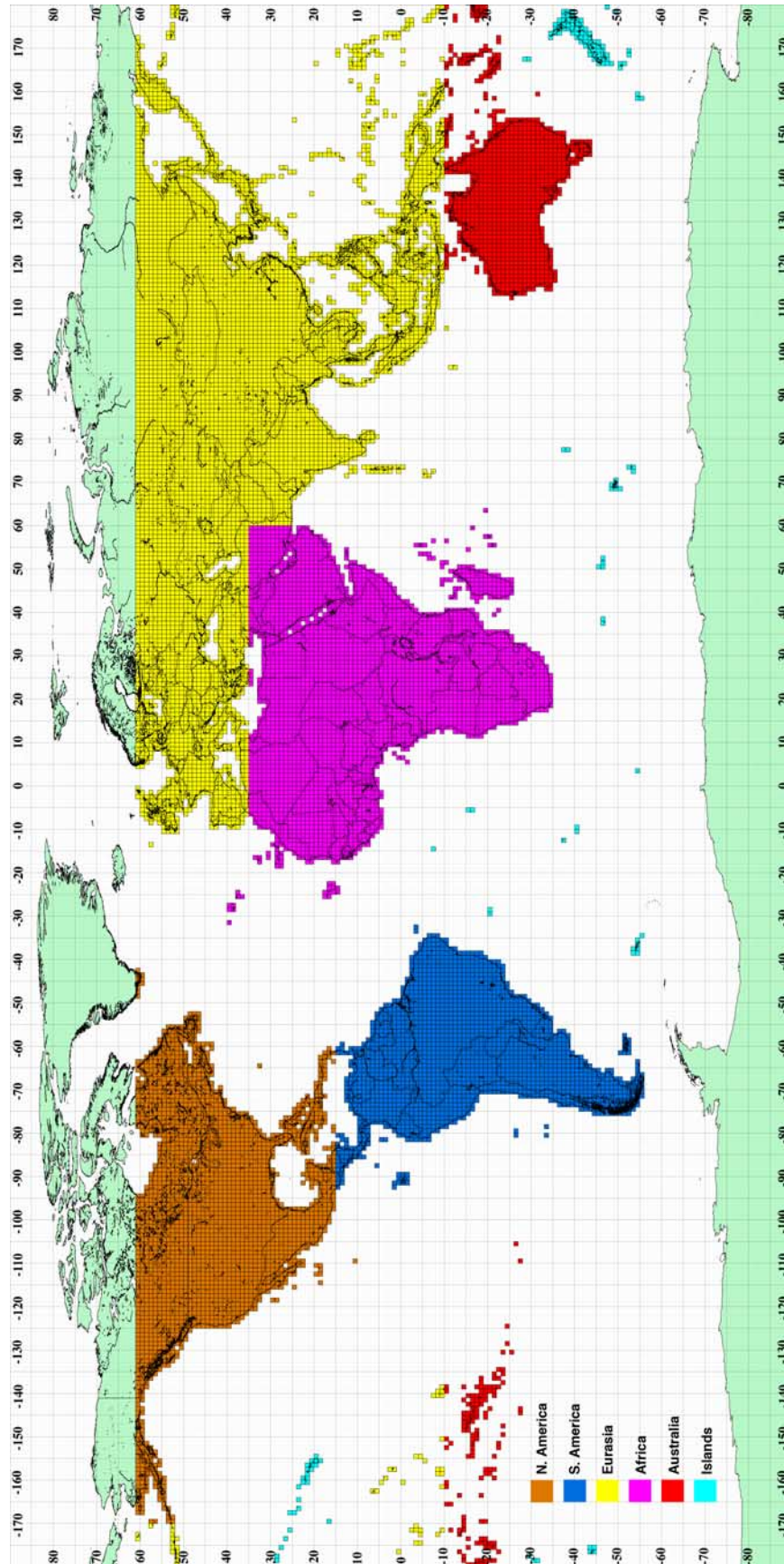


Figure 13. “Continents” defined for SRTM processing and bundle adjustments as well as for data distribution. Small grid shows $14,400 1^\circ \times 1^\circ$ cells used for distribution.

TABLE 1. Summary of SRTM Performance^a

	Africa	Australia	Eurasia	Islands	North America	South America
Absolute geolocation error	11.9	7.2	8.8	9.0	12.6	9.0
Absolute height error	5.6	6.0	6.2	8.0	9.0	6.2
Relative height error	9.8	4.7	8.7	6.2	7.0	5.5
Long-wavelength height error	3.1	6.0	2.6	3.7	4.0	4.9

^aAll quantities represent 90% errors in meters.

several schemes have been developed to fill voids. These void-filling algorithms fall into two general classes: interpolation and filling with data from other sources [e.g., *Grohman et al.*, 2006; *Hoffmann and Walter*, 2006]. Several commercial software packages make use of these algorithms.

[100] SRTM did not always map the true ground surface. Instead, it measured an effective height determined by the phase of the complex vector sum of all the returned signals from within the pixel being imaged. If the pixel contained bare ground, the phase reflected the height of the surface. If the ground was covered with vegetation, the return was influenced by the vegetation height, structure, and density. If the vegetation was dense enough, little or no signal returned from the ground below. Thus clear-cuts in dense forests or jungles are readily noticed. This effect has been exploited to derive tree heights by subtraction of “bare earth” DEMs (such as available from the U.S. Geological Survey (USGS)) from SRTM DEMs [*Simard et al.*, 2006; *Kellndorfer et al.*, 2004]. The offset in height between adjacent vegetated and unvegetated areas may not indicate accurately the height of the vegetation, however, as even the 5.6-cm wavelength of C radar often penetrated significantly into the vegetation canopy [*Carabajal and Harding*, 2006; *Hofton et al.*, 2006]. Schemes for correction of this vegetation bias have been proposed [e.g., *Carabajal and Harding*, 2006], but they rely on knowledge of the vegetation type and density and so remain a topic for research.

[101] Radar waves can also penetrate into frozen snow or ice or very dry soil, potentially up to several meters. Since SRTM flew in February, there was significant snow cover in the northern latitudes. Depending on the state of the snow, the C band–derived heights may be from the top of the snowpack or from the buried ground surface. Similarly, areas of very dry sand cover in the Sahara Desert, observed to be penetrated by L band (25 cm) by *Elachi et al.* [1984] and *Schaber et al.* [1986], may also be penetrated a short distance by the shorter wavelength C band system.

[102] Man-made objects, such as large buildings, roads, towers, and bridges are often problematic targets for radar imaging. Reflections, shadows, and smooth surfaces in built-up areas can often lead to severe layover, shadowing, and multipath artifacts. Given the 30- to 90-m posting of the SRTM data, only the largest man-made features are resolved, but the height of any urban SRTM pixel will be affected by the buildings within that pixel. Thus heights measured in cities will represent average building sizes rather than the height of the ground on which the buildings

sit. SRTM functioned very well in urban areas, and few artifacts are visible in the data.

5.2. C Radar Data Production

[103] The C radar data were processed at JPL over a period of 9 months by the Ground Data Processing System (GDPS) team. The GDPS production processing hardware comprised systems for radar data reformatting, topography processing, mosaic processing, automated quality analyses, and problem handling; a robotic tape library with 80-Tb near line data storage; workstations for visual quality analyses of the mosaicked height data; and a server for operations control and database management. GDPS processed and delivered the final data products by continent and island group (Figure 13).

[104] Because NASA and NGA had different requirements for final data products, 2 sets of SRTM data were produced. NGA required DTED specification products and also required several other data sets that were not furnished to NASA for public release. The NGA data products included: terrain height data, terrain height error data (THED), ascending and descending orthorectified image mosaics (OIM), and seam/hole composite maps all coregistered with the terrain height data.

[105] The terrain height data were furnished to NGA in DTED-2 format at 1×1 arc sec spacing up to latitude 50° and $1''$ (latitude) \times $2''$ (longitude) above 50° . A DTED-1 version, subsampled to 3×3 arc sec up to latitude 50° and $3''$ (latitude) \times $6''$ (longitude) above 50° was produced by NGA from the DTED-2 data. The Terrain Height Error Data file is an estimate of the random error. The seam-hole composite maps show the location of all data take boundaries and voids in the various data takes used in the mosaic.

[106] From the delivered SRTM DTED-2 data, NGA also produced a “finished” version with several improvements [*Slater et al.*, 2006]: Spikes and wells in the data were detected and voided out if they exceeded 100 m compared to surrounding elevations. Small voids (16 contiguous posts or less) were filled by interpolation of surrounding elevations; larger voids were left in the data. Water bodies were depicted in the finished data: The ocean elevation was set to 0 m, while lakes of 600 m or more in length were flattened and set to a constant height. Rivers that exceeded 183 m in width were delineated and monotonically stepped down in height. Islands were depicted if they had a major axis exceeding 300 m or the relief was greater than 15 m. This process resulted in the removal of a few $1^\circ \times 1^\circ$ cells from the original data set.

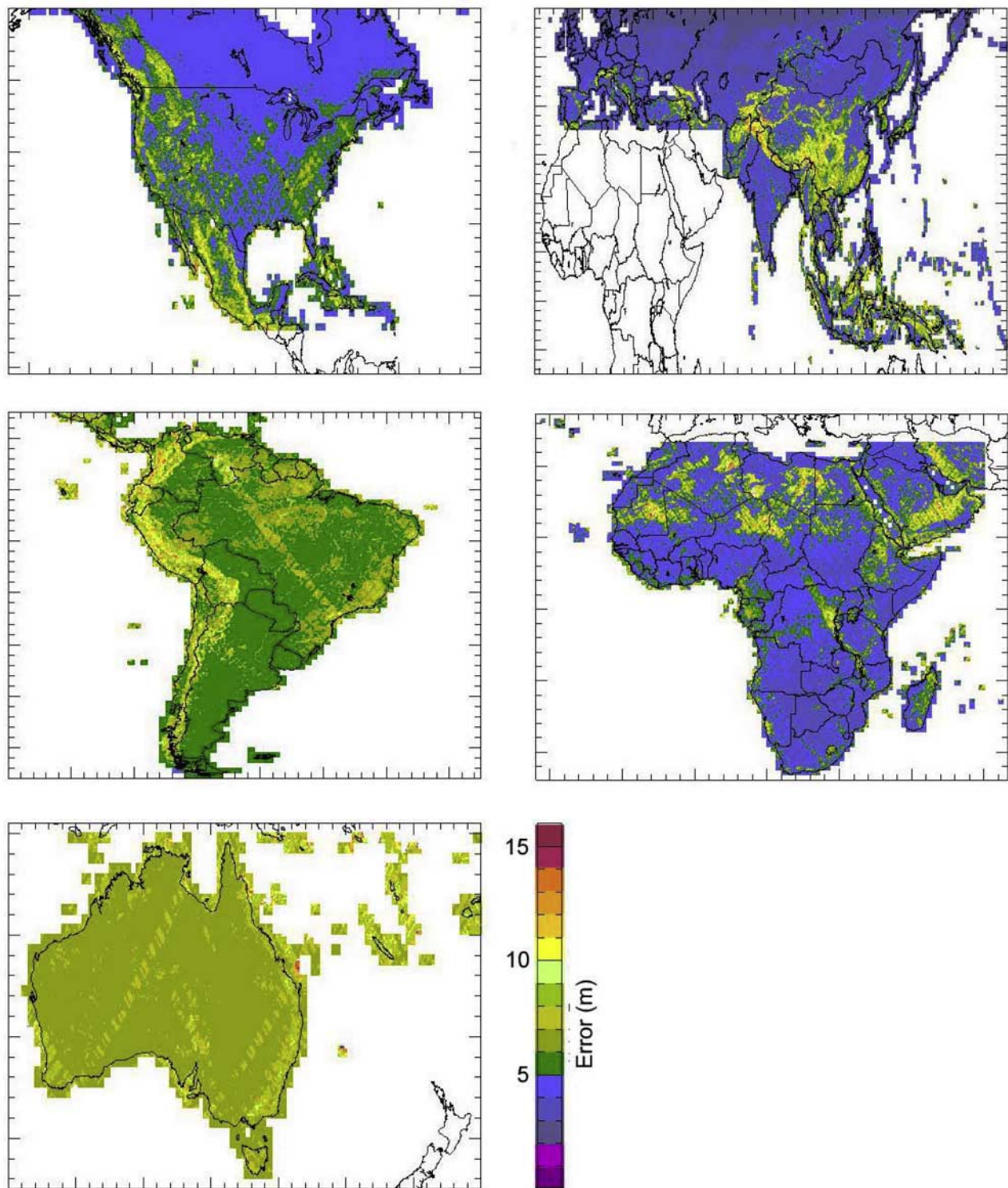


Figure 14. Absolute vertical errors for the five SRTM continents. Errors are less than about 10 m. Note larger errors for high-relief areas (Himalayas and Andes) and smooth areas (Sahara). From *Rodríguez et al.* [2005].

[107] In most cases the two orthorectified SRTM radar image mosaics at 1 arc sec resolution were available for identifying water bodies and delineating shorelines in each $1^\circ \times 1^\circ$ cell. These were used as the primary source for water body editing. The guiding principle for this editing

was that water must be depicted as it was in February 2000 at the time of the shuttle flight. A water layer derived from Landsat thematic mapper images up to 10 years old (Land-cover database) and medium-scale maps and charts were used as supplemental data sources, generally as supporting

TABLE 2. SRTM DEM Product Specifications

	C Radar	X Radar
Projection	none (“geographic”)	none (“geographic”)
Horizontal spacing	1 × 1 arc sec (~30 × 30 m) or 3 × 3 arc sec (~90 × 90 m) latitude/longitude	1 × 1 arc sec (~30 × 30 m) or 3 × 3 arc sec (~90 × 90 m) latitude/longitude
Vertical quantization	1 m	1 m
Horizontal reference	WGS84	WGS84
Vertical reference	EGM96 geoid	WGS84 ellipsoid
Data format	16-bit signed integer, IEEE byte order	16-bit signed integer, IEEE byte order
Void value	−32768	−32768
Wavelength	5.66 cm	3.1 cm
Bandwidth	10 MHz	10 MHz
Look angle	~30°–58°	54.5° (center)

evidence for water identified in the image mosaics. Since the Landcover water layer was derived mostly from Landsat 5 data collected a decade earlier than the shuttle mission and the map sources had similar currency problems, there were significant seasonal and temporal differences between the depiction of water in the ancillary sources and the actual extent of water bodies in February 2000. In rare cases, where the SRTM image mosaics were missing or unusable, Landcover was used to delineate the water in the SRTM cells.

[108] As a by-product of the finishing process a vector shoreline database (the SRTM Water Body Data set (SWBD)) was produced by NGA, which depicts all of the ocean coastlines, lake shorelines, and rivers. This database at full resolution along with full documentation from NGA on its production has been released to the public through the USGS.

[109] The NASA data products include DEMs at 1 × 1 arc sec (SRTM-1) and SRTM-3, which was produced by averaging 3 × 3 pixels (Table 2). A lower-resolution (30 arc sec), global data set called SRTM30 was produced from the USGS global topography model GTOPO30 (available at <http://edc.usgs.gov/products/elevation/gtopo30/gtopo30.html>) by averaging 30 × 30 pixels and replacing GTOPO30 pixels with SRTM data where possible. These version 1 products used “unfinished” SRTM data; version 2 of the NASA products incorporates the NGA finished data described above.

[110] The NASA data products are distributed to the public through the USGS EROS Data Center (see Table A1). Distribution of the C radar products is governed by a NASA/NGA Memorandum of Understanding. Briefly, raw data, full-resolution terrain height data, and strip DEMs with 1 arc sec spatial resolution for areas outside the territory of the United States are under the control of the Department of Defense. NASA and NGA are trying to work out a policy allowing access to 1 arc sec non-United States SRTM data for scientific use. The same types of data for areas within the United States and its possessions are not subject to restrictions. Distribution of terrain height data

with spatial resolution larger than or equal to 3 arc sec is not subject to restrictions. SRTM DTED-1 and DTED-2 data are also distributed by USGS with the same restrictions. The THED may also be released at a future date.

[111] Also processed and planned for public release as a NASA data product are orthorectified image data products. These will take the form of a separate file for each subswath that passes through a 1° × 1° cell (Figure 15). For each of the image files a file will be provided showing the local angle of incidence for each pixel. These products will allow studies of regional backscatter variations.

[112] The radar image product provides the mean surface backscatter coefficients of the mapped areas. This required the image processor to be radiometrically calibrated. For SRTM the goals for absolute and relative radiometric calibration were 3 dB and 1 dB, respectively. The SRTM main antenna was the major source of calibration error as it was a large active array antenna. In the spaceborne environment both zero gravity unloading and the large variation in temperature caused distortions in the phased array. Hundreds of phase shifters and transmit/receive modules populated the C band antenna panels. Monitoring the performance of each module was very difficult, causing inaccuracies in the antenna pattern predictions, in particular in elevation, as the beams were spoiled (defocused) to obtain a wide swath. Therefore antenna elevation pattern correction coefficients were derived with empirical methods using data taken over the Amazon rain forest. As the Amazon rain forest is a homogeneous and isotropic area, the backscatter coefficient is almost independent of the look angle. Without compensation, a scalloping effect would have been visible in the subswath and full swath images.

5.3. X Radar Data Production

[113] The X radar processing facility at the DLR consisted of the screening and transcription system, the InSAR processor, and the Geocoding and Mosaicking System (GeMoS) [Rabus et al., 2003]. These processing subsystems were independently operated, controlled by the DLR’s Data Information and Management System (DIMS). The intermediate data as well as the final products were stored and exchanged via a central archive.

[114] All X radar tapes were screened and the corresponding raw data were archived. The interferometric processor ingested raw data from each antenna and produced complex image pairs ready to form interferometric products. From these the interferogram of the unwrapped phase, the coherence map and the intensity image were generated. Motion compensation was subsequently applied to the unwrapped phase to correct effects caused by oscillations of the mast [Franceschetti et al., 2000]. The Geocoding and Mosaicking System converted the phase values to elevation information taking into account the shuttle’s orbit and attitude and the AODA-derived baseline vector. The geocoding step comprised the exact determination of the three-dimensional ground coordinates of each image

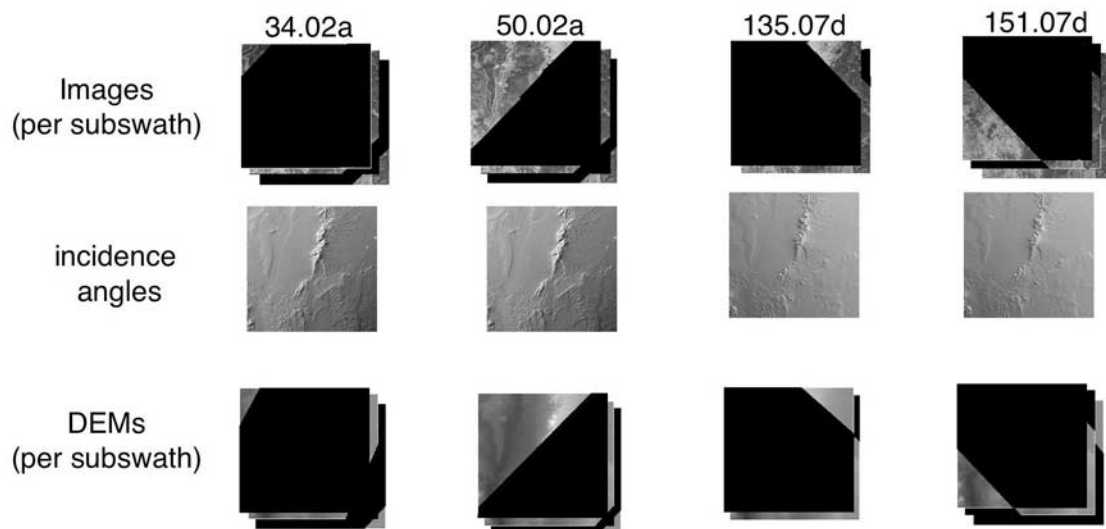


Figure 15. NASA image product. For a $1^\circ \times 1^\circ$ cell shown here, a file is created (top) for each subswath that crosses the cell. In this case, two ascending (labeled a) and two descending (labeled d) swaths cross the cell. For each of the swaths (middle) an image showing the local incidence angle at every pixel is also produced. Finally, the (bottom) DEM for each subswath is also produced. These data sets allow further study of SRTM performance and phenomenology.

pixel. This geometric transformation was applied to the elevation as well as image data and the coherence map.

[115] As with the C radar processing, the transformation of data from raw signal history to elevation was performed on each data take separately. The mosaicking process took into account adjacent and overlapping data takes, combining individual elevation models to a continuous large-area DEM. Finally, the DEM mosaic was split into $15' \times 15'$ tiles, transformed into DTED format and transferred to the archive.

[116] The DEM is provided in geographic coordinates. The delivery format is DTED. The elevation values refer to WGS84 both horizontally and vertically. This means that ellipsoidal heights are provided (Table 2). Additionally a height error map is available. It is coregistered to the DEM and describes the accuracy of each pixel based mainly on the coherence.

[117] Three different image products are offered, the single-look complex data set (SSC), the multilook ground range detected image (MGD), and the geocoded terrain-corrected product (GTC). Together with the GTC a geocoded incidence angle mask (GIM) is produced enabling radiometric corrections of the GTC's intensity values. The image products are available in the Committee on Earth Observation Satellites format. They cover an area of 150 km in azimuth and 50 km in range.

[118] The X radar data are archived and distributed using DLR's DIMS. It is a multimission system and consists of four major components, the product library (data catalog), ordering and production control, robot archive, and user information service including product delivery. Product delivery supports both media (CD) and internet. A user information system based on Java/World Wide Web tech-

nology enables querying and ordering. A map browser supports the definition of the search criteria (see Table A1).

6. EXAMPLES OF APPLICATIONS

[119] Since their release, SRTM data have found their way into many studies requiring topographic data. One ingenious application took advantage of the fact that the SRTM outboard antennas were positioned with a slight along-track baseline (approximately 7 m), making the interferometer sensitive to surface motion in the range of 0.1 m/s. *Romeiser et al.* [2002] and *Runge et al.* [2004] exploited this to make measurements of ocean currents using the X radar system. Other applications have been reported in many conferences and open literature papers. Of particular note was a workshop held in June 2005 and a resulting special issue of *Photogrammetric Engineering and Remote Sensing*, both centered on SRTM data validation and applications [Gesch et al., 2006a, 2006b]. In sections 6.1 and 6.2, two applications illustrating new avenues of research opened by the SRTM data set are described.

6.1. Geomorphology

[120] The new SRTM DEMs have probably had the largest impact on studies of regions in the developing world for which reliable, high-resolution digital topography was not previously available. With relatively few exceptions, nearly complete topographic coverage is now available for most of the nonpolar world and provides a foundation for a new analysis of diverse landscapes. Even where DEMs were previously available, the SRTM data provide a uniformity of quality and coverage that enables a more reliable

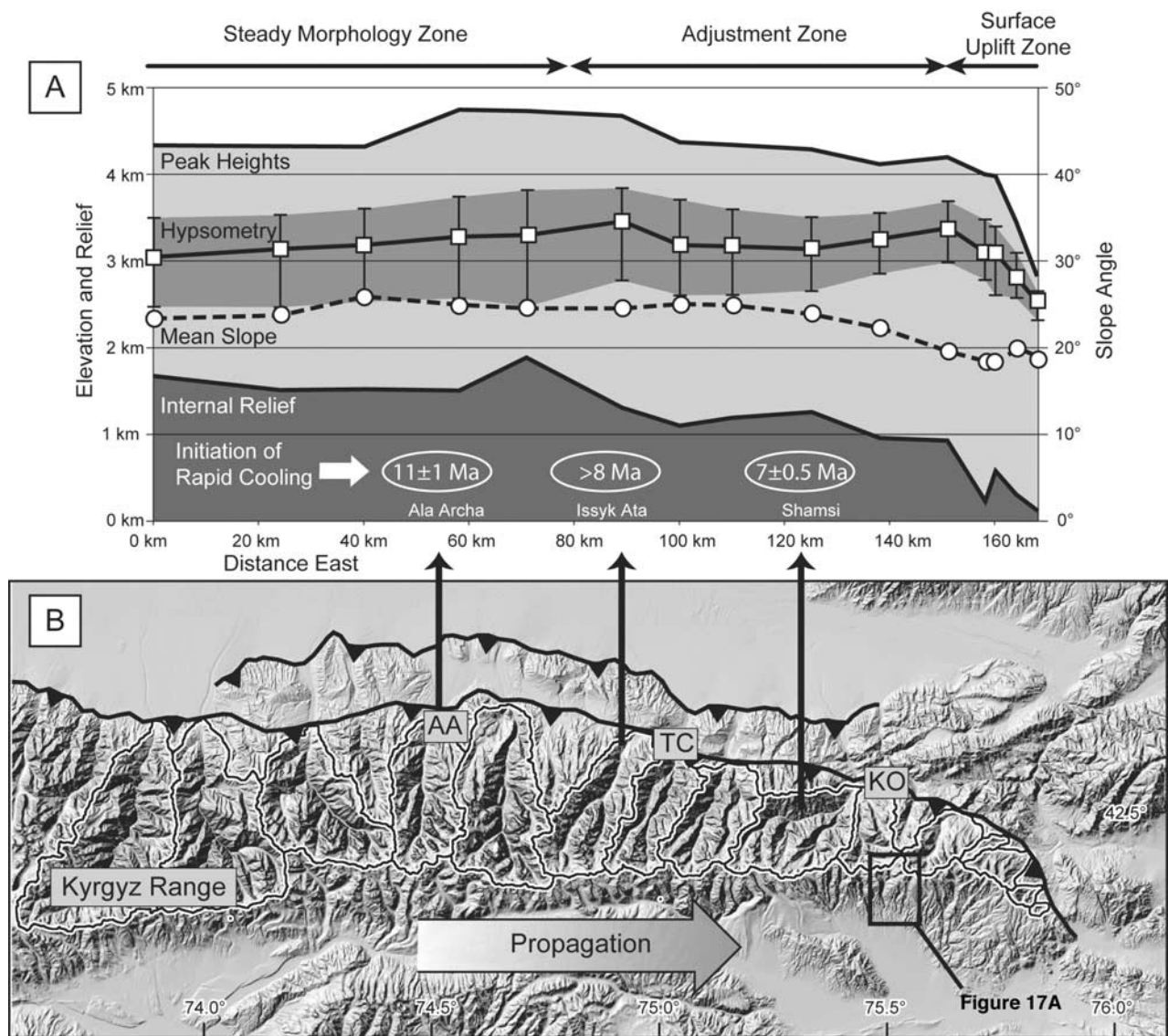


Figure 16. (a) Topographic characteristics of north facing basins along the length of the eastern half of the Kyrgyz Range. (b) Measured basins. Peak heights are highest elevations at the edge of each basin. Hypsometry shows median elevation bounded by 75th and 25th percentile elevations, shown with medium shading. Internal relief is measured as the difference between the highest and lowest elevations that are the same distance upstream from the basin outlet. The 75th percentile of the distribution of internal relief within each basin plotted with area beneath this curve is shown with dark shading. Surface uplift zone shows sharp increases in peak elevation, hypsometry, and internal relief from east to west in proportion to structural growth of the Kyrgyz Range. Adjustment zone shows progressive increases in mean slope angle, hypsometric range, and internal relief as north facing basins expand and incise uplifted bedrock. These morphometric indices approach constant values in the steady morphology zone. Basins plotted are AA, Ala Archa; TC, Tchuk; and KO, Komorchek. Modified after Sobel *et al.* [2006] and Oskin and Burbank [2007].

synthesis across broader regions irrespective of national boundaries.

[121] Over the past 2 decades, geologic and geomorphic studies have utilized digital topography in two general ways. The first is a straightforward analysis of topographic characteristics: mean, maximum, and minimum elevation; topographic relief, hypsometry (distribution of area versus elevation), and angles of hillslopes; gradients of river channels; and geometry of specific geomorphic features,

such as floodplains, alluvial fans, glacial moraines, or landslides. Such digital topographic description enables a previously unattainable quantification of landscape characteristics. For sites where the ergodic hypothesis (space-for-time substitution [see Chorley and Kennedy, 1971]) appears or is known to be valid, such data underpin new analyses of the evolution of landscapes. Consider the application of the SRTM DEM to a region that previously lacked a publicly accessible, high-resolution DEM: the Kyrgyz Range in

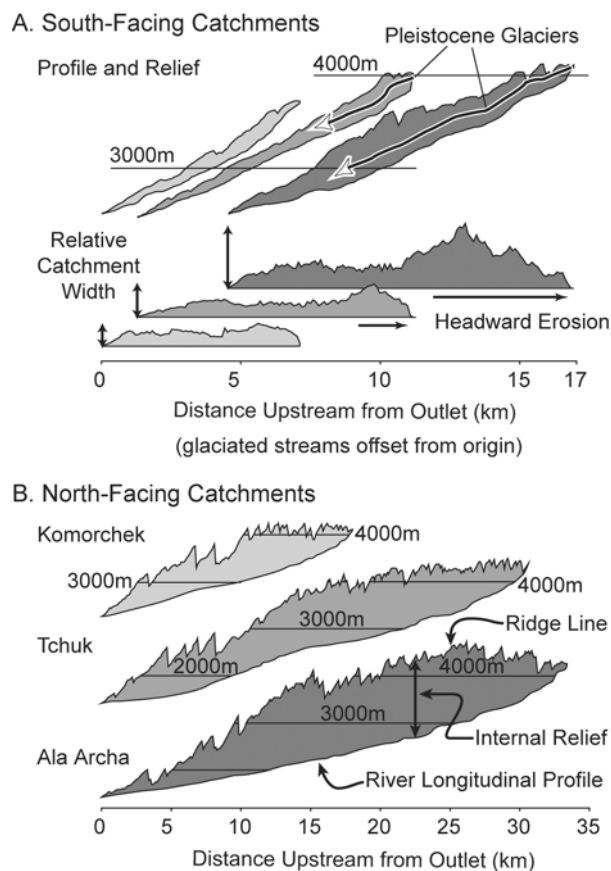


Figure 17. Comparisons of north and south facing catchment characteristics. See Figure 16 for locations. Internal relief is shown graphically as the shaded region between river longitudinal profile and equidistant ridge line elevations, where distance is measured up main and tributary streams to the divide. (a) South facing drainages in easternmost Kyrgyz Range illustrate morphologic changes that accompany incipient glacial erosion. Relative catchment width, shown for Figure 17a only, is a histogram of elevation points equidistant from the catchment outlet. Fluvial valleys resemble half-pipes with uniform catchment width and internal relief and with only slightly concave profiles. Glaciation causes headward erosion, increases internal relief and catchment width, and (except for the headwall area) creates a less steep valley bottom in the upper catchment. (b) Progressive expansion and deepening of north facing basins via glacial erosion at higher elevations and a combination of glacial and fluvial erosion at lower elevations. Komorchek lies at the transition from the surface uplift to the adjustment zone; Tchuk lies within the adjustment zone; Ala Archa lies within the steady morphology zone. Erosion of the transition zone is dominated by southward expansion of basins, probably via glacial cirque retreat. Prominent convexity in stream profile at Tchuk is a result of limited fluvial erosion downstream of glacially expanded valley. In the transition to steady morphology from Tchuk to Ala Archa the channel convexity is removed by fluvial and glacial incision that smoothes and lowers the longitudinal profile while increasing internal relief. Note that horizontal scale of Figure 17b is twice that of Figure 17a. Modified after Sobel *et al.* [2006] and Oskin and Burbank [2007].

northern Kyrgyzstan (Figure 16). At its highest point and near its center this range rises nearly 4 km above the adjacent foreland, the Chu Basin. The range crest descends toward the east, and fission track ages suggest the range has been propagating eastward over the past 10 Myr [Bullen *et al.*, 2001; Sobel *et al.*, 2006]. The Kyrgyz Range is unusual in that, prior to its Neogene growth, a regionally extensive unconformity surface had been beveled across the Paleozoic bedrock that now forms the core of the range. This erosion surface was subsequently buried beneath ~ 1 km of Cenozoic sediment. During range growth the striking contrast in erodibility between the Cenozoic strata and the Paleozoic bedrock caused the Cenozoic rocks to be readily stripped from the flanks of the range. In contrast, the erosion surface remained as a rather pristine marker that faithfully tracked the pattern of rock uplift [Burbank *et al.*, 1999; Oskin and Burbank, 2005].

[122] Progressive dissection of this uplifted unconformity surface is an ideal target for DEM analysis because erosion is expected to transform this initially planar surface into an integrated drainage network with associated topography. One topographic measure of dissection is “internal relief,” which defines the difference in elevation between all points at a given drainage distance from the outlet of a catchment. After a flow-routing routine defines the pathway of water across the landscape by connecting each pixel to the lowest-elevation pixel adjacent to it [Tucker and Slingerland, 1996], all pixels at each successive flow distance are compared. On more pristine parts of the surface, even after >2.5 km of rock uplift, initial drainages as defined with the SRTM DEM are analogous to half pipes that parallel the surface dip and have limited and rather uniform internal relief along their length (Figure 17). As dissection continues, fluvial drainages deepen and relief grows. As the range crest is elevated into the zone of glaciation, the SRTM DEM reveals that drainage characteristics are further transformed: The glaciated parts of the channel become less steep [Brocklehurst and Whipple, 2002], glaciers erode rapidly headward, and internal relief grows as the vertical separation between the valley floors and the adjacent ridge crests increases.

[123] A broader topographic perspective of the entire range (Figure 16) illuminates how the range has evolved during lateral propagation and progressive rock uplift. One can envision a simple growing fold that gains in altitude and relief as it propagates eastward. As erosion attacks this rather pristine, uplifted surface, progressive dissection of the fold gradually reshapes the surface and ultimately removes most topographic vestiges of the fold’s original geometry. Some measures of this transformation, as extracted from the SRTM DEM, include internal relief, hypsometry, peak elevations, and hillslope angles. Hypsometry is represented both by the mean elevation and by the first and third quartiles of the topography. Hillslope angles are measured across grids of 3×3 pixels (~ 270 m on a side). The easternmost 30 km of the range show an abrupt transformation as the unconformity surface is progressively dissected. Although the range crest at its easternmost point is nearly

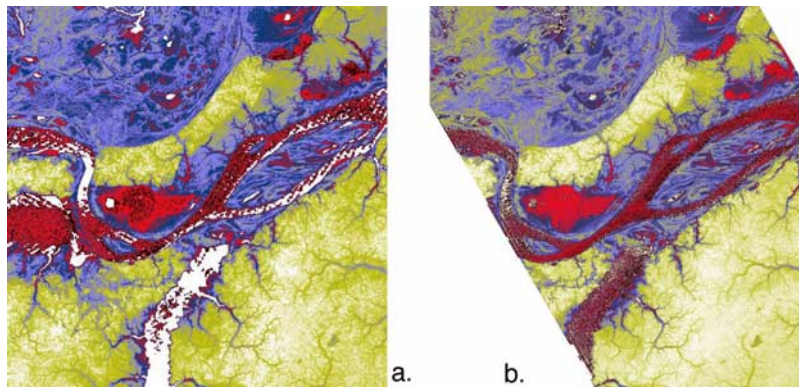


Figure 18. Images of water surface elevations from SRTM in the central Amazon Basin derived from the (a) C band and (b) X band systems. Compared to X band, C band elevations are missing (white areas) for some portions of the channel and lake areas. Elevation accuracies over water surfaces in both DEMs are degraded compared to surrounding land. Red represents the lowest elevations, followed by blue and yellow for the highest elevations. Scenes are about 50 km across. Modified from *LeFavour and Alsdorf* [2005].

3 km high, both the internal relief and the hypsometric range are small, indicating very limited dissection of this “youthful” uplift because of the bedrock’s resistance to erosion in the prevailing semiarid climate. Over the next 30 km to the west, topographic indices indicate rapid changes in erosion and rock uplift: The internal relief increases sixfold, whereas the hypsometric range more than doubles, and the mean elevation of the range crest increases by 40%.

[124] Although the rates of topographic change along the Krygyz Range are high near its eastern propagating tip (Figure 16), these rates abruptly decrease to the west of this zone. The ensuing consistency of mean elevations, despite an increase in peak heights, suggests that the range is approaching a topographic steady state, whereby rock uplift and erosion are balanced [Willet and Brandon, 2002]. Across this zone the internal relief and 25–75% hypsometric range increase as dissection becomes more pronounced,

and hillslopes steepen toward the topographic threshold for bedrock landsliding [Burbank et al., 1996]. Overall, these straightforward measures extracted from the SRTM DEM enable a quantification of topographic variability and, when combined with time constraints on propagation rates, illuminate the topographic evolution of the range.

[125] The second approach to geologic applications of DEMs uses derivative products from DEMs and may combine them with other data in order to provide insight on landscape processes. For example, when a drainage network is extracted from a DEM, the catchment area upstream of each pixel is readily defined. If the spatial distribution of rainfall across a landscape is then combined with upstream catchment areas, an estimate of water discharge can be calculated at each point in the landscape. Even without knowledge of rainfall patterns, the upstream area provides a reasonable proxy for discharge that can be readily derived from a DEM [de Roo, 1998]. A combination

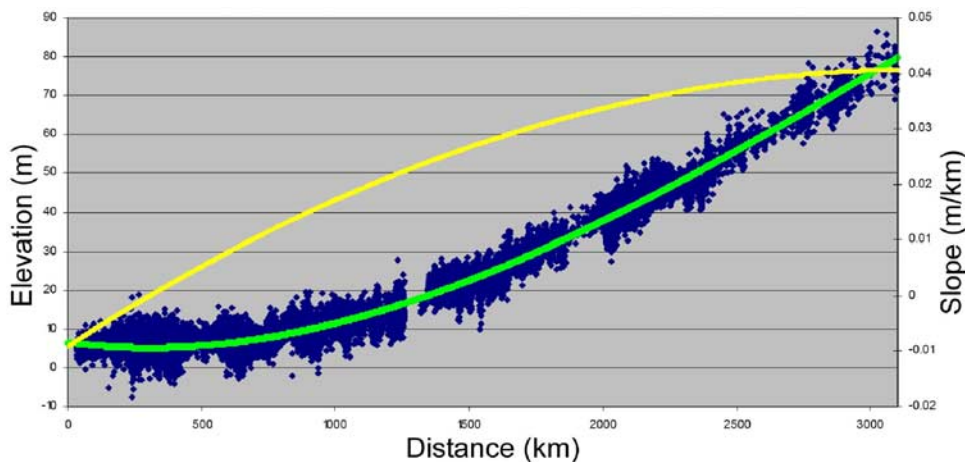


Figure 19. SRTM elevations (blue dots) and slope of the Amazon River. Third-order polynomial (green line) fit to elevation, h , along the main stem provides slope ($\partial h/\partial x$) (yellow line). Discharges estimated from slope match in situ stream gauge Q values to within 10%. Modified from *LeFavour and Alsdorf* [2005].

TABLE A1. SRTM-Related Web Links

	Link
SRTM Project	http://www.jpl.nasa.gov/srtm/
German Space Agency	http://www.dlr.de/srtm
Italian Space Agency	http://srtm.det.unifi.it/index.htm
Johnson Space Center STS-99	http://spaceflight.nasa.gov/shuttle/archives/sts-99/index.html
STS-99 Press Kit	http://www.shuttlepresskit.com/STS-99/index.htm
SRTM data access	http://www.jpl.nasa.gov/srtm/cbanddataproducts.html http://edc.usgs.gov/products/elevation.html http://seamless.usgs.gov/ http://glcf.umiacs.umd.edu/data/srtm/index.shtml http://srtm.csi.cgiar.org/
SRTM users' forum	http://pub7.bravenet.com/forum/537683448/
SRTM Workshop	http://edc.usgs.gov/conferences/SRTM/

of this discharge with the topographic slope of a channel yields an estimate of specific stream power: the amount of energy a river expends per unit area of its bed [Howard and Kerby, 1983]. Several studies have concluded that spatial variations in specific stream power can be correlated with variations in erosion rates [Whipple, 2004]. In tectonically active landscapes therefore the identification of areas characterized by high specific stream power can delineate tectonically active areas that are experiencing active deformation [Lavé and Avouac, 2001; Lavé and Burbank, 2004; Whipple, 2004]. Under circumstances where local calibration is available to define rates of deformation, such stream power analysis can be inverted to predict spatial variations in rock uplift rates [Kirby and Whipple, 2001], as long as rock strength is also spatially uniform. The availability of the SRTM DEM now permits rapid, global assessment of catchment areas and channel slopes, estimates of discharge, calculation of spatial variations in stream power, and predictions of variations in erosion rates [Finlayson et al., 2002; Lavé and Avouac, 2001].

[126] Climate analyses are also assisted by the SRTM DEM. For example, the combination of digital topography of mountain ranges with highly resolved maps of precipitation can highlight orographic controls on rainfall patterns. In glaciated alpine areas where paleoclimatic data are sparse, a combination of the SRTM DEM with satellite images or aerial photos permits a reconstruction of past variations in the regional snow line (equilibrium line altitude or ELA [Porter, 1975]) on former glaciers. The ELA represents the average elevation on a glacier for which accumulation and ablation are in balance when the glacier is in steady state. Commonly, about two thirds of the glacier lies in the accumulation area above the ELA at steady state. On remotely sensed images the outlines of former and present glaciers can be delineated and transferred to the DEM, from which the hypsometry for each glacier can be extracted. An ELA can then be calculated for each glacier by determining the altitude above which lies two thirds of the glacier. Contouring of these altitudes defines a three-dimensional ELA surface, and subtraction of the former ELA surface from the modern surface defines the amount of

ELA depression in the past [Porter, 1977]. Because winter snow accumulation and summer melting are the primary controls on the ELA, the modern gradient of the ELA provides insight on regional climate variability [Brozovic et al., 1997], whereas the difference between modern and ancient ELAs reflects changes in climate gradients over time [Burbank et al., 2003].

6.2. Hydrology

[127] Given our basic need for fresh water, among the most important hydrologic observations that can be made in a hydrologic basin are the temporal and spatial variations in water volumes stored in rivers, lakes, and wetlands [Alsdorf and Lettenmaier, 2003]. Changes in surface water storage (ΔS) and discharge (Q) are poorly known globally but are critical for constraining the terrestrial branch of the water cycle [Alsdorf et al., 2003]. To date, only SRTM has provided global measurements of both surface water area and elevation. However, little is known about the instrument performance for estimating ΔS and Q . The Amazon Basin is a particularly appealing target for remote sensing given its sparse gauge density, lack of continuous and reliable slope data that can be used in the estimation of discharge, and complexity of flow hydraulics.

[128] The spaceborne measurements required for understanding surface water hydraulics are the elevations of the water surface h and changes in elevations with space ($\partial h/\partial x$) and time ($\partial h/\partial t$) [Alsdorf and Lettenmaier, 2003]. Using Manning's equation, slope can be related to channel-constrained flow velocities and discharges, whereas $\partial h/\partial t$ over dynamic and complex wetlands provides ΔS . SRTM provides a one-time sampling of global h and $\partial h/\partial x$ values; a follow-on mission with strong SRTM heritage to continuously measure these hydraulic variables is in the initial planning stages (the Water Elevation Recovery Mission [Alsdorf and Lettenmaier, 2003; Alsdorf et al., 2007]).

[129] Because the SRTM C band antennae operated at about 30° to 58° look angles and the X band antennae operated at $\sim 54^\circ$, radar pulse returns from water surfaces are a function of roughening by wind or wave action. For a given roughness, shorter radar wavelengths produce greater backscatter than longer wavelengths. For example, comparisons of the river channel and lake water surfaces in Figure 18 demonstrate that X band elevations are available everywhere, whereas some portions of the C band DEM are missing h values. At about ± 5 m for C band and ± 20 m for X band the elevation accuracies over Amazonian water surfaces are much degraded compared to the surrounding terrestrial areas.

[130] Rather than an intrinsic measurement, water slopes are derived from elevation measurements collected by SRTM. Altimetric methods use the distance between orbits with the measured h values to calculate $\partial h/\partial x$; thus there is an inherent time step between h acquisitions that is built into the slope calculation [e.g., Birkett et al., 2002]. For gradually developing flood waves, such as the Amazon, such temporal discontinuities are minor. Because of the degraded

TABLE A2. SRTM-Related Acronyms

Acronym	Definition
ACS	antenna core structure
AFD	aft flight deck of space shuttle
AGDP	AODA ground data processor
AIRSAR	NASA/JPL airborne SAR test bed flown on NASA DC-8
AMS	antenna/mechanical system
AODA	Attitude and Orbit Determination Avionics, package on SRTM that measured the geometry of the radar interferometer
APC	AODA processing computers, laptop computers for storage, processing, and manipulation of AODA
ASI	Agenzia Spaziale Italiana, the Italian space agency
ASP	AODA support panel, support for AODA on the SRTM antenna
AST	autonomous star tracker, part of the AODA instrument suite
ASTROS	Advanced Stellar and Target Reference Optical Sensor, star tracker modified to track the LEDs of the OTA
ATMA	AODA telemetry monitor/analyzer, computers on the ground that accepted AODA data during the mission and processed it for rapid analysis
ATS	antenna trunnion structure, supported main antenna structure in shuttle payload bay, mechanically independent of the shuttle structure to avoid deformation of the antenna
ATT	ASTROS target tracker, modification of ASTROS to track OTA, part of AODA
BAT	beam autotracker, intended to compensate for fast movements of the mast (not used)
C band	radar wavelength of about 5 cm, SRTM C band operated at this wavelength
CEOS	Committee on Earth Observation Satellites, an international organization that helps develop standards for remote sensing data
CMS	Command Management Subsystem, part of the Mission Operations System
COR	CAL optical receiver, part of the fiber optic phase calibration system
CTTA	command timing and telemetry assembly
DDRE	digital data routing electronics, controlled SRTM data streams
Δv	delta velocity, change in shuttle velocity caused by rocket firings
DEM	digital elevation model, general name for topographic data represented digitally
DLR	Deutsches Zentrum für Luft- und Raumfahrt, the German space agency
DMS	Data Management Subsystem, part of the Mission Operations System
DOD	U.S. Department of Defense
DRIRU	dry-rotor inertial reference unit, type of gyroscope used as IRU on SRTM
DTED	digital terrain elevation data, specific format of DEM used by DOD; trademark NGA
EDM	electronic distance measurement, a surveying unit modified to measure SRTM mast length
ELA	equilibrium line altitude, elevation on a glacier at which accumulation and ablation are balanced
ERS	European Remote-Sensing Satellite, two-satellite series operating from 1991 until present, providing C band radar images and repeat-pass InSAR
ESA	European Space Agency
GDPS	ground data processing system, processed all SRTM C band data to DEMs
GIM	geocoded incidence-angle mask, X radar product depicting local incidence angles for each pixel
GIPSY	GPS Inferred Positioning System, set up by JPL to provide highly accurate GPS positions through postprocessing
GPS	Global Positioning System, system of satellite transmitters used for precise navigation
GTC	geocoded terrain-corrected product, orthorectified X radar image product
HEM	height error map, X radar product to go with their DEMs
InSAR	interferometric synthetic aperture radar, technique by which SRTM obtained topographic data, utilizes phase difference information from two radar antennas to precisely measure the radar imaging geometry
IRU	inertial reference unit, a gyroscope used as a continuous reference between star tracker and GPS solutions
JPL	Jet Propulsion Laboratory, a NASA center run by California Institute of Technology
JSC	Johnson Space Center, NASA center responsible for operation of the STS
KSC	Kennedy Space Center, NASA center responsible for shuttle launches
KuSP	Ku band signal processor, microwave link from shuttle to TDRS for high-rate data transmission
L band	radar wavelength of about 25 cm
MCC	Mission Control Center, main control center for shuttle flights at JSC, as seen on TV
MGD	multilook ground-range detected image, X radar image product not orthorectified (see GTC)
MOS	Mission Operations System, total system required to operate SRTM from launch to landing
MPOS	Mission Planning and Operations System, X radar mission operation system
MPS	Mission Planning Subsystem, part of the Mission Operations System
MSA	mission support area, at JSC, an office complex near MCC set up for high-level support of SRTM operations; at JPL, laboratories set up to download SRTM data and process it
NASA	National Aeronautics and Space Administration
NASDA	National Space Development Agency of Japan, now JAXA, Japan Aerospace Exploration Agency
NED	National Elevation Dataset, USGS-archived best digital elevation of United States
NGA	National Geospatial Intelligence Agency, part of Department of Defense
NIMA	National Imagery and Mapping Agency, formerly Defense Mapping Agency, became NGA in 2002
NMAS	National Map Accuracy Standards, defined by cartographers for scale, horizontal, and vertical precision and accuracy
OAS	outboard antenna structure
OASYS	outboard antenna system, all the systems at the end of the mast
OIM	orthorectified image mosaics, produced for NGA and not for public release, mosaics of the SRTM C band image data, one made up of ascending passes and one from descending passes
OOCO	on-orbit checkout, first phase of SRTM flight during which all systems were brought online, the mast was extended, and beams aligned
OSS	outboard support structure, supported outboard antennas and associated electronics at end of SRTM mast
OTA	optical target assembly, LED targets mounted on the end of the SRTM mast to allow tracking by ATT and measurement of mast motions
PES	Performance Evaluation Subsystem, part of the Mission Operations System

TABLE A2. (continued)

Acronym	Definition
PHRR	payload high-rate recorder, high-data-rate recorder for SRTM data
POCC	Payload Operations Control Center, main control center for SRTM payload, just down the hall from MCC
RIC	recorder interface controller, a laptop which operated the PHRR
RVS	radar verification system, accepted radar telemetry data during mission to verify performance
SAR	synthetic aperture radar, uses radar motion to synthesize a large antenna, thereby obtaining high resolution
ScanSAR	scanning synthetic aperture radar, electronically steers radar beam quickly enough to create a wide swath
SIR-A, -B, -C	Shuttle Imaging Radar series, flew in 1981, 1984, and 1994, respectively
SNR	signal-to-noise ratio, with noise fairly constant, low signal (backscattered radar) resulting in voids in the SRTM data
SRL	Space Radar Laboratory, another name for SIR-C/X-SAR
SRTM	Shuttle Radar Topography Mission, flew in 2000, the subject of this paper
STA	star tracker assembly, part of the AODA instrument suite
STS	Space Transportation System, full name of the space shuttle program
SWBD	SRTM water body database, produced as part of the NGA finishing process
TDRS	Tracking and Data Relay Satellite, system of communications satellites for relay of data from shuttle and other satellites to ground stations
THED	terrain height error data, depicts random errors in SRTM DEM
TMS	Telemetry Management Subsystem, part of the Mission Operations System
TOPSAR	topographic SAR, single-pass InSAR operating at C and L bands on NASA/JPL AIRSAR
USGS	U.S. Geological Survey
WGS84	World Geodetic System, 1984, one the main reference systems for cartography
X band	radar wavelength of about 3 cm, SRTM X-SAR operated at this wavelength

height accuracy, slopes calculated from SRTM require long reach lengths suitable for decreasing the noise. For example, in Figure 19 a polynomial is fitted to the extracted h values along most of the main stem Amazon River, which allows a simple derivative calculation [Hendricks and Alsdorf, 2004]. These SRTM-derived slopes also contain some temporal averaging related to the acquisitions over 10 days. Nevertheless, slopes compare well to ground truth and to radar altimetry measurements such that discharges at three Amazon River locations estimated from the SRTM slopes are within 10% of the observed in situ discharge Q .

7. SUMMARY

[131] SRTM was an example of engineering at its best; it marked a milestone in the field of remote sensing. In the span of 7 years the project evolved from concept to final data product, with 4 years of flight segment development, 10 days of observations, and 1 additional year of ground processor development. This was capped by 9 months of data production [Kobrick, 2006].

[132] Starting from the product requirements and some existing hardware, designers generated a rigorous allocation of errors across the system. Each contribution to the three-dimensional error in the height product was assessed, from phase noise and phase stability in the radar and its subsystems to the position and attitude of the shuttle and associated interferometer structures. Regular reviews of subsystem performance relative to error allocation and system cost, risk, and error budget trades were conducted during the development phase. The purpose was to ensure that the overall requirements could be met within the project plan. Ultimately, each subsystem worked within its allocation. The data products exceed specifications, as verified globally.

[133] As predicted before the mission, the success in automating the processing and calibration of a highly accurate product can be traced directly to the design of

the mission as a two-aperture single-pass interferometer in contrast to a repeat-pass scheme. One of the key factors in SRTM calibration was the ability to use ocean height as known ground control.

[134] In assessing the SRTM accomplishments it is important to acknowledge the experience gained from the many years of technology development and data analysis using JPL's AIRSAR/topographic SAR (TOPSAR), the first airborne interferometric topographic mapping system [Zebker et al., 1992]. Much of the theoretical understanding of interferometric system performance was verified using TOPSAR in the late 1980s and early 1990s, and indeed TOPSAR hardware improvements went hand in hand with theoretical developments. Algorithms and system specifications for SRTM have a direct heritage from TOPSAR. The SRTM processor was verified using TOPSAR data configured to SRTM formats.

[135] Radar interferometry represents a new remote sensing technique. In the same way, SRTM, as the first space-borne implementation of single-pass interferometry, represented a new class of remote sensing missions. In 10 days, SRTM mapped some of the least accessible regions of the world. The mission achieved what conventional cartography failed to achieve in 3 centuries of its existence: generation of a uniform-resolution, uniform-accuracy elevation model of most of the Earth's surface. By any standard, SRTM can be characterized as an unqualified success. In recognition of that success the mast and outboard systems (OASYS) are now displayed in the Udvar-Hazy Center of the Smithsonian Air and Space Museum.

APPENDIX A

[136] Table A1 lists web sites with additional information about SRTM as well as sites at which the data can be accessed. Table A2 is a comprehensive translation of acronyms used in this paper.

[137] **ACKNOWLEDGMENTS.** SRTM was the product of many people from many organizations. Particular thanks go to the crew of STS-99: Kevin Kregel, commander; Dom Gorie, pilot; and Mission Specialists Janice Voss, Janet Kavandi, Mamoru Mohri (NASDA), and Gerhard Thiele (ESA). The JSC MCC conducted the mission, and, in particular, the propellant team helped save many orbits of data taking through replanning of orbit trim maneuvers. Our colleagues at NGA were welcome additions to the team throughout the planning, design, and mission operations. Thanks also to three anonymous reviewers whose comments improved and streamlined this paper. Part of the research described in this paper was carried out at the Jet Propulsion Laboratory, California Institute of Technology, under contract with the National Aeronautics and Space Administration. DTED is a trademark of the National Geospatial-Intelligence Agency.

[138] The Editor responsible for this paper was Gerald North. He thanks one anonymous technical reviewer and one anonymous cross-disciplinary reviewer.

REFERENCES

- Alsdorf, D. E., and D. P. Lettenmaier (2003), Tracking fresh water from space, *Science*, 301, 1485–1488.
- Alsdorf, D., D. Lettenmaier, C. Vörösmarty, and The NASA Surface Water Working Group (2003), The need for global, satellite-based observations of terrestrial surface waters, *Eos Trans. AGU*, 84, 69.
- Alsdorf, D., E. Rodriguez, and D. Lettenmaier (2007), Measuring surface water from space, *Rev. Geophys.*, doi:10.1029/2006RG000197, in press.
- Attema, E. P. W. (1991), The Active Microwave Instrument on-board the ERS-1 satellite, *Proc. IEEE*, 79, 791–799.
- Bertiger, W. I., et al. (2000), Precise orbit determination for the Shuttle Radar Topography Mission using a new generation of GPS receiver, paper presented at ION GPS 2000, Inst. of Navig., Salt Lake City, Utah.
- Birkett, C. M., L. A. K. Mertes, T. Dunne, M. H. Costa, and M. J. Jasinski (2002), Surface water dynamics in the Amazon Basin: Application of satellite radar altimetry, *J. Geophys. Res.*, 107(D20), 8059, doi:10.1029/2001JD000609.
- Brocklehurst, S. H., and K. X. Whipple (2002), Glacial erosion and relief production in the eastern Sierra Nevada, California, *Geomorphology*, 42, 1–24.
- Brozovic, N., D. W. Burbank, and A. J. Meigs (1997), Climatic limits on landscape development in the northwestern Himalaya, *Science*, 276, 571–574.
- Bullen, M. E., D. W. Burbank, K. Y. Abdрахmatov, and J. Garver (2001), Late Cenozoic tectonic evolution of the northwestern Tien Shan: Constraints from magnetostratigraphy, detrital fission track, and basin analysis, *Geol. Soc. Am. Bull.*, 113, 1544–1559.
- Burbank, D. W., J. Leland, E. Fielding, R. S. Anderson, N. Brozovic, M. R. Reid, and C. Duncan (1996), Bedrock incision, rock uplift and threshold hillslopes in the northwestern Himalayas, *Nature*, 379, 505–510.
- Burbank, D. W., J. K. McLean, M. Bullen, K. Y. Abdрахmatov, and M. G. Miller (1999), Partitioning of intermontane basins by thrust-related folding, Tien Shan, Kyrgyzstan, *Basin Res.*, 11, 75–92.
- Burbank, D. W., A. E. Blythe, J. Putkonen, B. Pratt-Sitaula, E. Gabet, M. Oskin, A. Barros, and T. P. Ojha (2003), Decoupling of erosion and precipitation in the Himalayas, *Nature*, 426, 652–655.
- Carabajal, C., and D. J. Harding (2006), SRTM C-Band and ICESat laser altimetry elevation comparisons as a function of tree cover and relief, *Photogramm. Eng. Remote Sens.*, 72, 287–298.
- Chorley, R. J., and B. A. Kennedy (1971), *Physical Geography, A Systems Approach*, 370 pp., CRC Press, Boca Raton, Fla.
- Coltelli, M., G. Fornaro, G. Franceschetti, R. Lanari, M. Migliaccio, J. R. Moreira, K. P. Papathanassiou, G. Puglisi, D. Riccio, and M. Schwabisch (1996), SIR-C/X-SAR multifrequency multipass interferometry: A new tool for geological interpretation, *J. Geophys. Res.*, 101, 23,127–23,148.
- Defense Mapping Agency (1997), Department of Defense World Geodetic System 1984: Its definition and relationship with local geodetic systems, *Tech. Rep. TR 8350.2*, Natl. Imagery and Mapp. Agency, Washington, D. C. (Available at http://earth-info.nga.mil/GandG/publications/tr8350.2/tr8350_2.html)
- de Roo, A. P. J. (1998), Modeling runoff and sediment transport in catchments using GIS, *Hydrol. Processes*, 12, 905–922.
- Duncan, C., W. Bertiger, and L. Young (1998), GPS receivers for Shuttle Radar Topography Mission, paper presented at 54th Annual Meeting, Inst. of Navig., Denver, Colo.
- Duren, R. M., and E. F. Tubbs (2000), A modified commercial surveying instrument for use as a spaceborne rangefinder, paper presented at IEEE Aerospace Conference, Inst. of Electr. and Electron. Eng., Big Sky, Mont.
- Duren, R., E. Wong, B. Breckenridge, S. Shaffer, C. Duncan, E. Tubbs, and P. Salomon (1998), Metrology, attitude, and orbit determination for spaceborne interferometric synthetic aperture radar, *Proc. SPIE Int. Soc. Opt. Eng.*, 3365, 51–60.
- Elachi, C. (1988), *Spaceborne Radar Remote Sensing: Applications and Techniques*, IEEE Press, Piscataway, N. J.
- Elachi, C., et al. (1982), Shuttle Imaging Radar Experiment, *Science*, 218, 996–1004.
- Elachi, C., L. E. Roth, and G. G. Schaber (1984), Spaceborne radar subsurface imaging in hyperarid regions, *IEEE Trans. Geosci. Remote Sens.*, 22, 383–388.
- Elachi, C., J. B. Cimino, and M. Settle (1986), Overview of the Shuttle Imaging Radar-B preliminary results, *Science*, 232, 1511–1516.
- Evans, D. L., J. J. Plaut, and E. R. Stofan (1997), Overview of the spaceborne imaging radar-C/X-band synthetic-aperture radar (SIR-C/X-SAR) missions, *Remote Sens. Environ.*, 59, 135–140.
- Falorni, G., V. Teles, E. R. Vivoni, and R. L. Bras (2005), Analysis and characterization of the vertical accuracy of digital elevation models from the Shuttle Radar Topography Mission, *J. Geophys. Res.*, 110, F02005, doi:10.1029/2003JF000113.
- Farr, T. G., and M. Kobrick (2000), Shuttle Radar Topography Mission produces a wealth of data, *Eos Trans. AGU*, 81, 583–585.
- Fielding, E. J., C. L. Werner, T. G. Farr, and G. F. Peltzer (1995), Geomorphic applications of digital elevation models derived from ERS-1 and SIR-C SAR interferometry, *Eos Trans. AGU*, 76, 64.
- Finlayson, D. P., D. R. Montgomery, and B. Hallet (2002), Spatial coincidence of rapid inferred erosion with young metamorphic massifs in the Himalayas, *Geology*, 30, 219–222.
- Foni, A., and D. Seal (2004), Shuttle Radar Topography Mission: An innovative approach to shuttle orbital control, *Acta Astron.*, 54, 565–570.
- Franceschetti, G., A. Iodice, S. Maddaluno, and D. Riccio (2000), Effect of antenna mast motion on X-SAR/SRTM performance, *IEEE Trans. Geosci. Remote Sens.*, 38, 2361–2372.
- Gesch, D., M. Oimoen, S. Greenlee, C. Nelson, M. Steuck, and D. Tyler (2002), The National Elevation Dataset, *Photogramm. Eng. Remote Sens.*, 68, 5–11.
- Gesch, D., T. G. Farr, J. Slater, J-P. Muller, and S. Cook (2006a), New products from the Shuttle Radar Topography Mission, *Eos Trans. AGU*, 87, 174.
- Gesch, D., J-P. Muller, and T. G. Farr (2006b), The Shuttle Radar Topography Mission—Data validation and applications, foreword to special issue, *Photogramm. Eng. Remote Sens.*, 72, 233–234.
- Geudtner, D., M. Zink, C. Gierull, and S. Shaffer (2002), Interferometric alignment of the X-SAR antenna system on the space Shuttle Radar Topography Mission, *IEEE Trans. Geosci. Remote Sens.*, 40, 995–1006.
- Goldstein, R. M. (1995), Atmospheric limitations to repeat-track radar interferometry, *Geophys. Res. Lett.*, 22, 2517–2520.

- Goldstein, R. M., H. A. Zebker, and C. Werner (1988), Satellite radar interferometry: Two-dimensional phase unwrapping, *Radio Sci.*, *23*, 713–720.
- Grohman, G., G. Kroenung, and J. Strebeck (2006), Filling SRTM voids: The delta surface fill method, *Photogramm. Eng. Remote Sens.*, *72*, 213–216.
- Guth, P. L. (2006), Geomorphometry from SRTM: Comparison to NED, *Photogramm. Eng. Remote Sens.*, *72*, 269–277.
- Hall, O., G. Falconi, and R. L. Bras (2005), Characterization and quantification of data voids in the Shuttle Radar Topography Mission data, *IEEE Geosci. Remote Sens. Lett.*, *2*, 177–181.
- Ham, A. (2005), A standardized approach to phase unwrap detection/removal and void fill of the Shuttle Radar Topography Mission (SRTM) data, paper presented at SRTM–Data Validation and Applications Workshop Reston, Va., 14–16 June. (Available at <http://edc.usgs.gov/conferences/SRTM/>)
- Hendricks, G., and D. Alsdorf (2004), Channel slopes on Amazon Basin rivers from the SRTM DEM, *Eos Trans. AGU*, *85*(47), Fall Meet. Suppl., Abstract H23E-1178.
- Hoffmann, J., and D. Walter (2006), How complementary are SRTM-X and -C band digital elevation models?, *Photogramm. Eng. Remote Sens.*, *72*, 261–268.
- Hofton, M., R. Dubayah, J. B. Blair, and D. Rabine (2006), Validation of SRTM elevations over vegetated and non-vegetated terrain using medium footprint lidar, *Photogramm. Eng. Remote Sens.*, *72*, 279–285.
- Holzner, J., and R. Bamler (2002), Burst-mode and scanSAR interferometry, *IEEE Trans. Geosci. Remote Sens.*, *40*, 1917–1934.
- Howard, A., and G. Kerby (1983), Channel changes in badlands, *Geol. Soc. Am. Bull.*, *94*, 739–752.
- Jordan, R. L., B. L. Huneycutt, and M. Werner (1995), The SIR-C/X-SAR synthetic aperture radar system, *Trans. IEEE Geosci. Remote Sens.*, *33*, 829–839.
- Kellndorfer, J., W. Walker, L. Pierce, C. Dobson, J. A. Fites, C. Hunsaker, J. Vona, and M. Clutter (2004), Vegetation height estimation from Shuttle Radar Topography Mission and national elevation datasets, *Remote Sens. Environ.*, *93*, 339–358.
- Kiel, B., D. Alsdorf, and G. LeFavour (2006), Capability of SRTM C- and X-band DEM data to measure water elevations in Ohio and the Amazon, *Photogramm. Eng. Remote Sens.*, *72*, 313–320.
- Kirby, E., and K. Whipple (2001), Quantifying differential rock-uplift rates via stream profile analysis, *Geology*, *29*, 415–418.
- Kobrick, M. (2006), On the toes of giants—How SRTM was born, *Photogramm. Eng. Remote Sens.*, *72*, 206–210.
- Lavé, J., and J. P. Avouac (2001), Fluvial incision and tectonic uplift across the Himalaya of central Nepal, *J. Geophys. Res.*, *106*, 26,561–26,591.
- Lavé, J., and D. W. Burbank (2004), Denudation processes and rates in the Transverse Ranges, southern California: Erosional response of a transitional landscape to external and anthropogenic forcing, *J. Geophys. Res.*, *109*, F01006, doi:10.1029/2003JF000023.
- LeFavour, G., and D. Alsdorf (2005), Water slope and discharge in the Amazon River estimated using the Shuttle Radar Topography Mission digital elevation model, *Geophys. Res. Lett.*, *32*, L17404, doi:10.1029/2005GL023836.
- Lemoine, F. G., et al. (1998), The development of the Joint NASA GSFC and National Imagery and Mapping Agency (NIMA) Geopotential Model EGM96, NASA Tech. Publ. TP-1998–206861, Goddard Space Flight Cent. Greenbelt, Md. (Available at <http://cddis.gsfc.nasa.gov/926/egm96/egm96.html>)
- Madsen, S. N., and H. A. Zebker (1998), Imaging radar interferometry, in *Principles and Applications of Imaging Radar; Manual of Remote Sensing*, vol. 2, edited by F. M. Henderson and A. J. Lewis, chap. 6, pp. 359–380, John Wiley, Hoboken, N. J.
- Massonnet, D. (1997), Satellite radar interferometry, *Sci. Am.*, *276*, 46–53.
- Massonnet, D., and K. L. Feigl (1995), Discrimination of geophysical phenomena in satellite radar interferograms, *Geophys. Res. Lett.*, *22*, 1537–1540.
- McWatters, D. A., G. Lutes, E. Caro, and M. Tu (2001), Optical calibration phase locked loop for the Shuttle Radar Topography Mission, *IEEE Trans. Instrum. Meas.*, *50*, 40–46.
- Moreira, J., et al. (1995), X-SAR interferometry: First results, *IEEE Trans. Geosci. Remote Sens.*, *33*, 950–956.
- Oskin, M., and D. W. Burbank (2005), Alpine landscape evolution dominated by cirque retreat, *Geology*, *33*, 933–936.
- Oskin, M., and D. W. Burbank (2007), Transient landscape evolution of basement-cored uplifts: Example of the Kyrgyz Range, Tien Shan, *J. Geophys. Res.*, doi:10.1029/2006JF000563, in press.
- Porter, S. C. (1975), Equilibrium-line altitudes of late Quaternary glaciers in the Southern Alps, New Zealand, *Quat. Res.*, *5*, 27–47.
- Porter, S. C. (1977), Present and past glaciation threshold in the Cascade Range, Washington, U. S. A.: Topographic and climatic controls, and paleoclimatic implications, *J. Glaciol.*, *18*, 101–116.
- Rabus, B., M. Eineder, A. Roth, and R. Bamler (2003), The shuttle radar topography mission—A new class of digital elevation models acquired by spaceborne radar, *J. Photogramm. Remote Sens.*, *57*, 241–262.
- Raney, R. K. (1998), Radar fundamentals: Technical perspective, in *Principles and Applications of Imaging Radar; Manual of Remote Sensing*, vol. 2, edited by F. M. Henderson and A. J. Lewis, chap. 2, pp. 9–130, John Wiley, Hoboken, N. J.
- Rodriguez, E., C. S. Morris, J. E. Belz, E. C. Chapin, J. M. Martin, W. Daffer, and S. Hensley (2005), An assessment of the SRTM topographic products, *JPL Publ.*, *D31639*, 143 pp.
- Rodriguez, E., C. S. Morris, and J. E. Belz (2006), A global assessment of the SRTM performance, *Photogramm. Eng. Remote Sens.*, *72*, 249–260.
- Romeiser, R., H. Breit, M. Eineder, and H. Runge (2002), Demonstration of current measurements from space by along-track SAR interferometry with SRTM data, paper presented at IEEE International Geoscience and Remote Sensing Symposium 2002, Inst. Electr. and Electron. Eng., Toronto, Ont., Can.
- Rosen, P. A., S. Hensley, I. R. Joughin, F. K. Li, S. N. Madsen, E. Rodriguez, and R. M. Goldstein (2000), Synthetic aperture radar interferometry, *Proc. IEEE*, *88*, 333–382.
- Ruffino, G., A. Moccia, and S. Esposito (1998), DEM generation by means of ERS tandem data, *IEEE Trans. Geosci. Remote Sens.*, *36*, 1905–1912.
- Runge, H., S. Suchandt, H. Breit, M. Eineder, J. Schulz-Stellenfeth, J. Bard, and R. Romeiser (2004), Mapping of tidal currents with SAR along-track interferometry, paper presented at IEEE International Geoscience and Remote Sensing Symposium 2004, Inst. of Electr. and Electron. Eng., Anchorage, Alaska.
- Sansosti, E., R. Lanari, G. Fornaro, G. Franceschetti, M. Tesauro, G. Puglisi, and M. Coltelli (1999), Digital elevation model generation using ascending and descending ERS-1/ERS-2 tandem data, *Int. J. Remote Sens.*, *20*, 1527–1547.
- Schaber, G. G., J. F. McCauley, C. S. Breed, and G. R. Olhoeft (1986), Shuttle imaging radar: Physical controls on signal penetration and subsurface scattering in the eastern Sahara, *IEEE Trans. Geosci. Remote Sens.*, *24*, 603–623.
- Simard, M., K. Zhang, V. H. Rivera-Monroy, M. S. Ross, P. L. Ruiz, E. Castaneda-Moya, R. R. Twilley, and E. Rodriguez (2006), Mapping height and biomass of mangrove forests in Everglades National Park with SRTM elevation data, *Photogramm. Eng. Remote Sens.*, *72*, 299–311.
- Slater, J. A., G. Garvey, C. Johnston, J. Haase, B. Heady, G. Kroenung, and J. Little (2006), The SRTM data ‘finishing’ process and products, *Photogramm. Eng. Remote Sens.*, *72*, 237–247.
- Smith, B., and D. Sandwell (2003), Accuracy and resolution of shuttle radar topography mission data, *Geophys. Res. Lett.*, *30*(9), 1467, doi:10.1029/2002GL016643.
- Sobel, E. R., M. Oskin, D. Burbank, and A. Mikolaichuk (2006), Exhumation of basement-cored uplifts: Example of the Kyrgyz

- Range quantified with apatite fission track thermochronology, *Tectonics*, 25, TC2008, doi:10.1029/2005TC001809.
- Tucker, G. E., and R. Slingerland (1996), Predicting sediment flux from fold and thrust belts, *Basin Res.*, 8, 329–349.
- Werner, M. (2001), Shuttle Radar Topography Mission (SRTM), Mission overview, *J. Telecomm.*, 55, 75–79.
- Whipple, K. X. (2004), Bedrock rivers and the geomorphology of active orogens, *Annu. Rev. Earth Planet. Sci.*, 32, 151–185.
- Willett, S. D., and M. T. Brandon (2002), On steady states in mountain belts, *Geology*, 30, 175–178.
- Wong, E., W. Breckenridge, D. Boussalis, P. Brugarolas, D. S. Bayard, J. Spanos, and G. Singh (2001), Post-flight attitude reconstruction for the Shuttle Radar Topography Mission, paper presented at AAS/AIAA Conference, Am. Astronaut. Soc., Quebec City, Que., Can.
- Zebker, H. A., and R. M. Goldstein (1986), Topographic mapping from interferometric synthetic aperture radar observations, *J. Geophys. Res.*, 91, 4993–4999.
- Zebker, H. A., S. N. Madsen, J. Martin, K. B. Wheeler, T. Miller, Y. Lou, G. Alberti, S. Vetrella, and A. Cucci (1992), The TOP-SAR interferometric radar topographic mapping instrument, *IEEE Trans. Geosci. Remote Sens.*, 30, 933–940.
- Zebker, H. A., C. Werner, P. A. Rosen, and S. Hensley (1994), Accuracy of topographic maps derived from ERS-1 interferometric radar, *IEEE Trans. Geosci. Remote Sens.*, 32, 823–836.
- Zebker, H. A., P. A. Rosen, and S. Hensley (1997), Atmospheric effects in interferometric synthetic aperture radar surface deformation and topographic maps, *J. Geophys. Res.*, 102, 7547–7563.
-
- D. Alsdorf, Department of Geological Sciences, Ohio State University, Columbus, OH, 43210-1308, USA.
- D. Burbank, Department of Earth Science, University of California, Santa Barbara, Santa Barbara, CA 93106-1100, USA.
- E. Caro, R. Crippen, R. Duren, T. G. Farr, S. Hensley, M. Kobrick, M. Paller, E. Rodriguez, P. A. Rosen, L. Roth, D. Seal, S. Shaffer, J. Shimada, and J. Umland, Jet Propulsion Laboratory, California Institute of Technology, Pasadena, CA 91109-8099, USA. (tom.farr@jpl.nasa.gov)
- M. Oskin, Department of Geological Sciences, University of North Carolina, Chapel Hill, NC 27599, USA.
- M. Werner, Deutsches Zentrum für Luft- und Raumfahrt, D-82230, Wessling, Germany.